




Brownian translation and rotation from the ballistic to the diffusive limit and derivation of the physical properties of dust agglomerates

Ben Schubert ^{1,*}, Noah S. Molinski ¹, Ingo von Borstel,¹ Thilo Glißmann,¹ Daniyar Balapanov,²

Andrei Vedernikov ² and Jürgen Blum ¹

¹*Technische Universität Braunschweig, Institute of Geophysics and extraterrestrial Physics, Mendelssohnstr. 3, 38106 Braunschweig, Germany*

²*Université Libre de Bruxelles, Microgravity Research Center, CP 165/62 Avenue F.D. Roosevelt 50, 1050 Brussels, Belgium*

 (Received 15 September 2022; revised 13 February 2023; accepted 24 February 2023; published 23 March 2023)

We analyzed the translational and rotational Brownian motion of aggregates of micrometer-sized silica spheres under microgravity conditions and in rarefied gas. The experimental data was collected in the form of high-speed recordings using a long-distance microscope as part of the ICAPS (Interactions in Cosmic and Atmospheric Particle Systems) experiment on board of the sounding rocket flight Texus-56. Our data analysis shows that the translational Brownian motion can be used to determine the mass and translational response time of each individual dust aggregate. The rotational Brownian motion additionally provides the moment of inertia and the rotational response time. A shallow positive correlation between mass and response time was found as predicted for aggregate structures with low fractal dimensions. Translational and rotational response times are roughly in agreement. Using the mass and the moment of inertia of each aggregate, we determined the fractal dimension of the aggregate ensemble. Slight deviations from the pure Gaussian one-dimensional displacement statistics were found in the ballistic limit for both the translational and rotational Brownian motion.

DOI: [10.1103/PhysRevE.107.034136](https://doi.org/10.1103/PhysRevE.107.034136)

I. INTRODUCTION

The history of the thermal motion of massive particles actually begins in botany. As early as 1828, Brown observed with a simple light microscope that flower pollen grains floating in a drop of water moved suddenly and irregularly [1]. The physical explanation for this phenomenon was given decades later by Einstein [2] and also by Smoluchowski [3]. Finally in 1930, Uhlenbeck and Ornstein could mathematically prove the fundamental solution to the stochastic process of Brownian motion [4].

The mathematical starting point to describe the Brownian motion of dust particles in the ICAPS (Interactions in Cosmic and Atmospheric Particle Systems) experiments is the Ornstein-Fürth relation [4]

$$\langle \Delta x^2 \rangle = 2 \Delta t \frac{kT \tau_t}{m} \left(1 - \frac{\tau_t}{\Delta t} + \frac{\tau_t}{\Delta t} e^{-\Delta t / \tau_t} \right), \quad (1)$$

which represents the one-dimensional mean-squared displacement $\langle \Delta x^2 \rangle$ experienced by a dust particle with mass m during the time interval Δt , with k , T , and τ_t being Boltzmann's constant, the gas and dust temperature (assumed to be equal), and the translational response time (or friction time) of the dust particle to the gaseous environment, respectively. In the free molecular flow regime, the translational response time is proportional to the ratio between mass and geometrical cross section of the dust particle [5].

Analogous to Eq. (1), the rotational Brownian motion can be described by the relation

$$\langle \Delta \theta^2 \rangle = 2 \Delta t \frac{kT \tau_r}{I} \left(1 - \frac{\tau_r}{\Delta t} + \frac{\tau_r}{\Delta t} e^{-\Delta t / \tau_r} \right), \quad (2)$$

with $\langle \Delta \theta^2 \rangle$ being the mean-squared angular displacement of a rotating particle during the time interval Δt , with I and τ_r being the moment of inertia of the dust particle with respect to its momentary rotation axis and its rotational response time, respectively.

For short times $\Delta t \ll \tau_t$ and $\Delta t \ll \tau_r$, Eqs. (1) and (2) can be approximated by their ballistic limits

$$\langle \Delta x^2 \rangle = (\Delta t)^2 \frac{kT}{m} \quad (3)$$

and

$$\langle \Delta \theta^2 \rangle = (\Delta t)^2 \frac{kT}{I}, \quad (4)$$

respectively. In this limit, the mean particle speed is given by

$$\langle v \rangle = \sqrt{\frac{\langle \Delta x^2 \rangle}{(\Delta t)^2}} = \sqrt{\frac{kT}{m}}, \quad (5)$$

whereas the mean angular velocity reads

$$\langle \omega \rangle = \sqrt{\frac{\langle \Delta \theta^2 \rangle}{(\Delta t)^2}} = \sqrt{\frac{kT}{I}}. \quad (6)$$

With this, the mean one-dimensional translation and rotation energies read $\langle E_t \rangle = \frac{1}{2} m \langle v \rangle^2$ and $\langle E_r \rangle = \frac{1}{2} I \langle \omega \rangle^2$, respectively.

*b.schubert@tu-bs.de

In contrast, for very long times, $\Delta t \gg \tau_t$ and $\Delta t \gg \tau_r$, Eqs. (1) and (2) become

$$\langle \Delta x^2 \rangle = 2 \Delta t \frac{kT \tau_t}{m} = 2 D_t \Delta t \quad (7)$$

and

$$\langle \Delta \theta^2 \rangle = 2 \Delta t \frac{kT \tau_r}{I} = 2 D_r \Delta t, \quad (8)$$

i.e., the classical diffusion equations, with the diffusion constants for translation

$$D_t = \frac{kT \tau_t}{m} \quad (9)$$

and rotation

$$D_r = \frac{kT \tau_r}{I}, \quad (10)$$

respectively.

In an experimental approach, the ICAPS campaign tries to overcome previous difficulties of losing the dust cloud on rather short timescales due to minuscule temperature gradients in the gas, which lead to thermophoretic drift motion of the entire dust cloud. This is achieved by actively controlling and restoring the position of the dust cloud using a thermophoretic dust-cloud manipulation system [6]. On top of that, ICAPS allows us to study the transition from the fully developed ballistic to the fully developed diffusive Brownian motion with a large number of particles.

Earlier work by our group on the Brownian motion of dust aggregates as an experimental simulation of the conditions in protoplanetary disks has always used the same technique, namely, dispersing a cloud of dust particles and small aggregates thereof under microgravity conditions (drop towers, sounding rockets, and orbital experiments, respectively) into rarefied gas [5,7–9]. The latter is a prerequisite for a realistic simulation of the gaseous environment of protoplanetary disks for which the gas flow around the dust particles is always in the free-molecular flow regime, i.e., the mean-free path of the gas molecules is much larger than the size of the dust grains considered. Observations have been performed by no-invasive optical long-distance microscopy combined with high-speed imaging techniques. In the earliest study [5], we found that this technique is feasible to derive quantitative information about the particle motion. Thereupon, we investigated how dust aggregates grow due to ballistic Brownian motion [7,8]. A further experimental study with increased temporal resolution could resolve the translational Brownian motion in the transition from the ballistic [Eq. (3)] to the diffusive limit [Eq. (7)] and could also quantitatively describe the Brownian rotation of microrods [9].

In this paper, we aim at resolving the full range from ballistic to diffusive Brownian motion, both for its translational and rotational components. As we will do this for the identical aggregates, we can derive the mass (m) and the moment of inertia (I) as well as the translational (τ_t) and rotational response time (τ_r) independently of each other for every particle. From the knowledge of m and I , one can derive the radius of inertia

$$r_g = \sqrt{\frac{I}{m}}, \quad (11)$$

which reveals important structural information of the dust aggregates.

When dust grains of identical individual radii r_0 and mass m_0 agglomerate, the forming aggregates are often fractal in nature, i.e., they follow the relation

$$\frac{m}{m_0} = \beta \left(\frac{r_g}{r_0} \right)^{d_f}, \quad (12)$$

with the so-called fractal dimension d_f and a scaling parameter β . Using Eqs. (11) and (12), one can then derive these parameters as well.

II. EXPERIMENTAL DETAILS

The ICAPS philosophy is to disperse a cloud of initially individual dust particles into a rarefied N₂ atmosphere. The gas pressure is chosen to mimic the rarefied gas kinetics of a protoplanetary disk, i.e., the Knudsen number with respect to the individual dust grains has to be much larger than unity. This also means that in a terrestrial laboratory, the dust grains sediment to the ground at relatively high speed, so a long undisturbed observation of Brownian motion is impossible. Thus, the ICAPS experiment was performed onboard the sounding rocket Texus-56 in November 2019 as part of a campaign of the European Space Agency. In the following subsections, we will describe the experimental setup, the dust sample, and the procedures during the ICAPS flight.

A. Experimental setup

To simulate as realistically as possible the conditions during early planet formation, the dust particles were injected into a rarefied N₂ gas atmosphere with a pressure of 56 Pa, and in a second experiment run with a pressure of 67 Pa. The dust particles were deagglomerated and injected into the gaseous environment using a rapidly spinning cogwheel [10]. To avoid loss of the dust cloud by any type of residual acceleration, we used a cloud manipulation system (CMS) [6], which compensates any global residual acceleration to facilitate long observation times. Two mutually perpendicular overview cameras with a field-of-view of $\sim 1.5 \text{ cm}^2$ and a pixel resolution of $\sim 12 \text{ }\mu\text{m}$ measured the 3D cloud position with a frequency of 50 Hz. This continuous tracking was used by the CMS as input for a feedback loop, which generated the compensation force to keep the cloud quiescent in the observation volume. The active element of the CMS was a set of fast Peltier elements, arranged in a coaxial four-ring geometry. The dust particles can be attracted or repelled by the Peltier elements due to the effect of thermophoresis and the thermal creep flow, with both forces being collinear. The arrangement of the Peltier elements allowed the CMS to create a three-dimensional force that translates the cloud at constant velocity without deformation, since the thermophoretic velocity in the free-molecular flow regime is independent of the particle size or agglomeration status [11,12].

To observe the motion of the dust aggregates, the ICAPS setup used a combination of a long-distance microscope (LDM) and high-speed imaging techniques. The optical resolution of the LDM was $\sim 1 \text{ }\mu\text{m}$ and its depth-of-focus was a few 10 μm . The particles were imaged by a high-speed

TABLE I. Comparison of the derived physical properties of particle 1 in Fig. 1 with all particles from data set T2 (mass and translational friction time τ_t) and data set R2 (moment of inertia and rotational friction time τ_r). The reference to data sets T2 and R2 can be found in Fig. 23 in Appendix G.

Property	Particle 1	All particles	Unit
Mass	2.5×10^{-13}	$3 \times 10^{-15} - 4 \times 10^{-12}$	kg
No. of monomers	78	1–1000	
Moment of inertia	1.5×10^{-23}	$1 \times 10^{-25} - 4 \times 10^{-22}$	kg m^2
τ_t	9.2×10^{-3}	$4 - 25 \times 10^{-3}$	s
τ_r	10.1×10^{-3}	$1 - 13 \times 10^{-3}$	s

camera with a region-of-interest of 1024×1024 pixels, a continuous recording speed of 1000 frames per second, a pixel resolution of $1 \mu\text{m}/\text{pixel}$, i.e., a field of view of $1 \text{ mm} \times 1 \text{ mm}$, and a bright-field LED illumination.

B. Dust sample

The particles used in ICAPS were monodisperse SiO_2 particles with radii $r_0 = 0.725 \pm 0.030 \mu\text{m}$ [13] (Sicstar type 43-00-153). Their physical properties are detailed in Blum and Schr apler [14] (their Table 1). As the mean-free paths of the N_2 gas molecules were $126 \mu\text{m}$ for a pressure of 56 Pa and $105 \mu\text{m}$ for a pressure of 67 Pa, the Knudsen numbers with respect to the monomer grains were $\text{Kn} = 168 \gg 1$ and $\text{Kn} = 140 \gg 1$ for the two experimental runs, respectively. In this case, the free-molecular flow limit of the hydrodynamic interaction between gas and solid particles applies.

Analysis of the injected dust cloud showed that the number density of the monomer grains throughout the experimental runs was on the order of $3 - 6 \times 10^{12} \text{ m}^{-3}$. With a monomer-grain mass of $3.2 \times 10^{-15} \text{ kg}$, this yields an average mass density in the range of $0.01 - 0.02 \text{ kg/m}^3$. With gas densities of $6.3 \times 10^{-4} \text{ kg/m}^3$ and $7.5 \times 10^{-4} \text{ kg/m}^3$ in the two experiments, the density ratio between solids and gas was on the order of 15–30. Effects of this high mass loading on the Brownian motion of nearby particles could, however, not be investigated, due to the relative large interparticle distances ($>100 \mu\text{m}$) and the smallness of the depth of focus of the LDM.

Due to a slight electric charging of the particles upon injection, an initial rapid agglomeration phase of the monomer grains into aggregates containing up to ~ 1000 monomer grains was observed. The Coulomb interactions between neighboring aggregates had no influence on their Brownian motion due to their large mean separation distance of $\gtrsim 100 \mu\text{m}$. Thus, in this paper we describe the Brownian motion of these aggregates. Examples of the dust aggregates are shown in Fig. 1. In the Appendix, we will show examples of our Brownian motion analysis for particle 1 in Fig. 1. The derived properties of this aggregate are summarized in Table I along with the same properties of all aggregates in the sample.

C. Experimental procedure

During the flight with the high-altitude rocket Texus-56, a little more than 360 seconds of microgravity time were

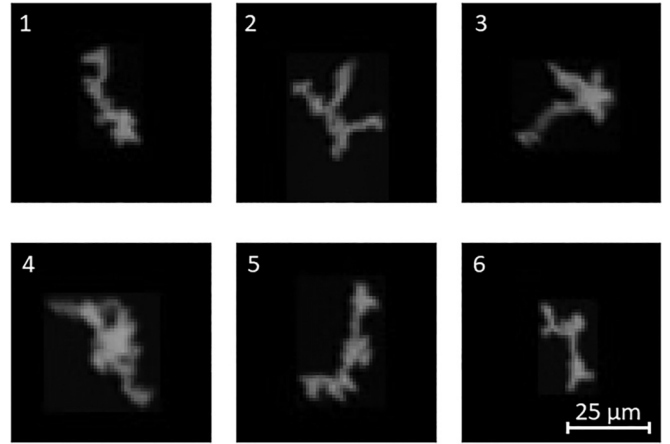


FIG. 1. Example of the dust aggregates used for the translational and rotational Brownian motion analysis. Due to the observation principle of bright-field microscopy, particles in the raw images are darker than the background. For the purpose of analysis, the images have been flat-field corrected, effectively inverting them and removing illumination patterns (see Appendix F3). In the upper left frame, particle 1 can be seen, which is used as example in the Appendix.

achieved. During these six minutes, a total of two particle-cloud injections could be performed, which are therefore treated as two separate experimental runs in the data analysis. The cloud was lost due to a software bug after about 220 s, so a new experiment run starting with an injection was initiated manually via telecommand.

After the injection of the particle cloud, the experiment was set to run a sequence of several different modes (e.g., charge measurements). For the analysis of Brownian motion, however, we used only undisturbed phases, i.e., the CMS levitation mode during which no external fields were applied, apart from those counteracting ensemble drifts (overall cloud motion). Figure 2 shows that the impact of the latter on the single-particle trajectories is negligible. The undisturbed phases collectively span 187 112 LDM images (approximately 187 s of total duration, i.e., roughly half of the microgravity time available). Of these images, 124 107 are from the first and 63 005 are from the second experiment run.

D. Observation of Brownian motion and data extraction

The analysis of the Brownian motion of the dust aggregates present in the ICAPS flight on Texus-56 is based on the 187 112 LDM images from the undisturbed phases mentioned above. Apart from occasional CMS operations (see Sec. III for a discussion of the noise level caused by the CMS), all particles are almost entirely free from any external disturbances, so any derived particle motion can be attributed to Brownian translational and rotational motion, i.e., a stochastic interaction with the ambient rarefied gas.

In the first step of the data extraction, a flat-field correction was applied to the raw images (see Appendix F3). The particles on each image were then localized using a connected-component analysis with a threshold of four counts [15]. For each particle, a bounding box was created before the particle center was determined from the image moments

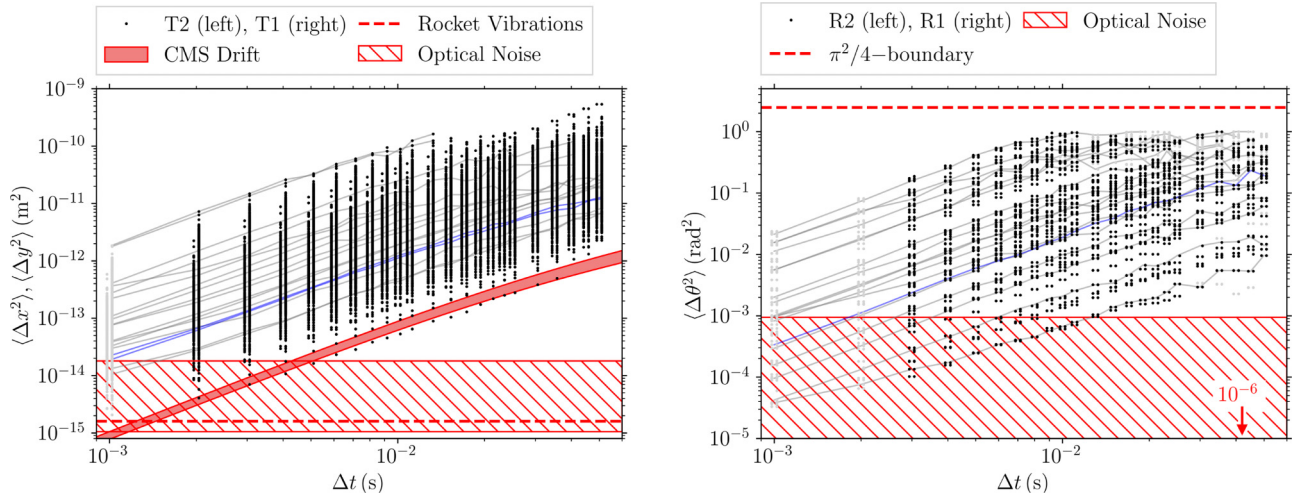


FIG. 2. Left: $\langle \Delta x(j)^2 \rangle$ and $\langle \Delta y(j)^2 \rangle$ values as a function of $\Delta t(j)$ for all measured particles (data points). The symbols are slightly offset to the right (left) for data set T1 (data set T2). Gray symbols were not used to fit Eq. (1). The gray curves connect data points that belong to the same particle for an exemplary subset including particle 1 from Fig. 1, which is shown in blue. The red curved band denotes the noise level caused by the CMS. The hatched horizontal band marks the noise level caused by the discretization of the aggregate images, the shot noise, and illumination flickering by the LDM light source (see Appendix F3). The dashed line denotes the estimated upper limit of noise caused by vibrations of the rocket, as discussed in Appendix F6. Right: Rotational equivalent to left panel for all particles in data sets R1 and R2. The hatched band marks the shot noise and illumination flickering by the LDM light source (see Appendix F3). The dashed line denotes the boundary imposed by the maximum unambiguous rotation angle of $\theta = \pi/2$ rad (see Sec. IID).

of the cropped image. The trajectories of the particles were then determined using a Crocker and Grier tracking algorithm [16,17]. At this stage of the analysis, the output for each particle consisted of a unique ID, the x, y coordinates of the center of extinction for every image of the particle, and the coordinates of the bounding box, respectively. Also, we implemented a measure of sharpness, for which we compiled a sorted statistic of the absolute pixel-to-pixel gradients in x and y directions in a given cropped particle image. The 84% quantile, i.e., where the gradient statistic exceeds 1σ , is then our measure of sharpness (for each image of each particle). This criterion appeared to be much more consistent than other methods (e.g., the standard deviation after convolution with a Laplacian or the brightness-to-area ratio) and is therefore considered to be sufficient for our purposes. Further data, mostly unused in this paper, included the optical radius of inertia, the total extinction, and the total pixel number (or area) for each particle image.

With this data set, we then started the filtering process. For the analysis of Brownian motion, perturbations in the gas flow have to be kept to a minimum. Therefore, we selected only undisturbed experimental phases, i.e., during the levitation mode of the CMS. We then excluded segments from the particle tracks in those time frames in which not all of the particle was visible, i.e., where the bounding box touched the image edge, retaining the original IDs. Next, we dropped all particle tracks consisting of less than 100 usable images, which we regarded as the minimum number of frames for a statistical analysis. At this point, the data set consisted of 1367 particles, which we used for the translational Brownian motion analysis.

For the rotational analysis, however, more filtering steps were needed, because the requirements for the particle sharpness are higher than in the translational case. We chose only

those particles for further Brownian rotation analysis, which made up an area of at least 50 pixels and had a sharpness of at least 10 (see above) for at least 100 frames. For smaller or fainter particles, any elongation became indiscernible, which is crucial in the next steps. This subset was then further filtered by hand for sufficient ellipticity as all rotational parameters would be derived from fitting ellipses to the particle contours. The ellipse fitting procedure, which used a threshold of 20 counts to get a contour of the sharpest region, then yielded the angle of rotation with respect to the vertical center axis and the ellipse center, as well as the lengths of the semimajor and semiminor axes, leaving us with 77 particles for the rotational analysis.

At this point, we had compiled two data sets, with the one for the rotational analysis being a full subset of the translational data set. For both data sets, we proceeded as follows: First, the displacements in the two spatial directions (x and y) were calculated independently for different time steps Δt , with $\Delta t = 1 - 10$ ms in 1 ms increments, $\Delta t = 11 - 25$ ms in 2 ms increments, and $\Delta t = 30 - 50$ ms in 5 ms increments, respectively. Then, for each Δt value and for a minimum number of 20 data points, a normalized cumulative frequency plot of the displacements was made and the standard deviations σ_x and σ_y were determined by using an error integral fit. More details on how these fits were applied can be found in Sec. III A.

We set $\langle \Delta x^2 \rangle = \sigma_x^2$ (same for the y component) and applied to these mean-squared standard deviations a fit of Eq. (1), which has only the particle mass and the translational friction time as fit parameters. However, since the data points for $\Delta t = 1$ ms often showed considerable deviations from the expected trend [$\langle \Delta x^2 \rangle \propto (\Delta t)^2$, see Fig. 13 in Appendix A for an example], this value was always ignored. One reason for this deviation might be that the uncertainty in the determi-

nation of the difference in particle position is maximal at the smallest Δt values [18].

The quality of each fit is here represented by a modified residual sum of squares

$$\text{RSS}_{t,x} = \frac{1}{J} \sum_{j=j_0}^{j_{\max}} (\log_{10}(\langle \Delta x(j)^2 \rangle) - \log_{10}(\Gamma(\Delta t(j), m_x, \tau_{t,x})))^2, \quad (13)$$

where $\Gamma(\Delta t(j), m_x, \tau_{t,x})$ is the right-hand side of Eq. (1). The logarithmic values have been used to avoid overrepresentation of $\langle \Delta x(j)^2 \rangle$ values at large Δt . Also, the RSS has been normalized by the number of data points included in the fit $J = j_{\max} - j_0$, with j_0 and j_{\max} being the indices of the first and last data point used, to allow us to draw comparisons between particles.

The same procedure was also applied to the analysis of the rotational Brownian motion, replacing Γ with the right-hand side of Eq. (2) and $\langle \Delta x(j)^2 \rangle$ with $\langle \Delta \theta(j)^2 \rangle$ in Eq. (13) to yield an RSS_r . However, as the maximum unambiguous rotation angle is $\Delta \theta = \pi/2$, we restricted the data to mean-squared rotation angles of $\langle \Delta \theta^2 \rangle \leq \pi^2/4$. Still, the tracks used for the rotational analysis can sometimes become too short for proper resolution at high Δt values, since they are reduced to mostly in-focus segments, despite a minimum length of 100 frames. Therefore, the last data point used in the fit (j_{\max}) is chosen by hand in these cases. Also, the data points at $\Delta t = 1$ ms and $\Delta t = 2$ ms were ignored to achieve a better fit.

Then, finally, the normalized RSS_t of the chosen fits were used to filter out 589 particles with a maximum RSS_t in both spatial directions of 0.004. We further constrained the data set to a maximum relative error of the mass resulting from the fit of 10% (see Fig. 18 in Appendix C), which left us with 362 particles. These data make up the first translational data set T1. If the same margin of error is assumed for the translational friction time, we get data set T2 with 172 particles. Since the quality of the friction time is irrelevant for comparing measurements of mass and moment of inertia, we derived the first rotational data set R1 from T1. Here, only those particles were included for which a RSS_r of less than 0.006 was achieved in the rotational analysis. Also, a threshold for the relative error of the moment of inertia was applied, though it was set to a more lenient 50% due to the challenges of rotational measurements. This resulted in 65 particles in data set R1. For the purpose of comparing translational and rotational friction times, we finally applied a 10% margin of error to τ_t as in data set T2 and a 50% margin of error to τ_r and get 55 particles in total in data set R2. The procedures, data sets, and particle numbers are summarized in Fig. 23 in Appendix G.

III. DATA ANALYSIS

A. Analysis of the translational Brownian motion

From the recorded tracks (see Fig. 10 in Appendix A as an example for particle 1), the two-dimensional positions x_i and y_i of each particle were determined for all available time stamps $t_i = i \Delta t_0$, with $\Delta t_0 = 1$ ms and $i = 0, \dots, N$. As the two spatial dimensions are physically independent of each other, the subsequent analysis was done for each of the di-

mensions. In the following, we will only consider the spatial dimension x . The analysis for y is completely analogous.

We calculated one-dimensional displacement data through

$$\Delta x_i(j) = x_{i+j} - x_i, \quad (14)$$

with

$$\Delta t(j) = j \Delta t_0 \quad (15)$$

and $j = 1, 2, 3, \dots, n$; $i = 0, j, 2j, \dots, nj$. Thus, we derived one-dimensional displacement arrays with lengths $\sim \frac{N}{j}$. From statistical mechanics and thermodynamics, it follows that the $\Delta x_i(j)$ should obey a Gaussian distribution. To prove this for our dust aggregates and to determine the mean-squared displacement $\langle \Delta x_i(j)^2 \rangle$ required for the application of Eq. (1), we size-sorted the $\Delta x_i(j)$ values for each $\Delta t(j)$ from the smallest (negative) value to the largest (positive) value [hereafter, the arrays $\Delta x(j)$ and $\Delta x'(j)$], accumulated their number, normalized the total to unity, and fitted error integrals, i.e.,

$$\Phi(\Delta x(j)) = \frac{1}{\sqrt{2\pi\sigma_x^2(j)}} \int_{-\infty}^{\Delta x(j)} e^{-\frac{(x'(j)-\delta_x(j))^2}{2\sigma_x(j)^2}} d\Delta x'(j), \quad (16)$$

to the normalized cumulative histograms with the two fit parameters $\sigma_x^2(j) \equiv \langle \Delta x_i^2(j) \rangle$ and $\delta_x(j) \equiv \langle \Delta x_i(j) \rangle$, respectively, the latter being a measure for a possible systematic drift of the particles (see Appendix D). Figure 12 in Appendix A shows examples of the fits for dust aggregate 1 and various values of Δt .

To visualize how close the particle displacements of all particles in our sample follow a Gaussian, we normalized the one-dimensional displacement values $\Delta x_i(j)$ according to

$$\xi_{G,x}(j) = \frac{\Delta x_i(j) - \delta_x(j)}{\sigma_x(j)}, \quad (17)$$

so all particles should follow the same normalized error integral:

$$\Phi(\xi_G(j)) = \frac{1}{\sqrt{2\pi}} \int_{-\infty}^{\xi_G(j)} e^{-\frac{\xi_G'(j)^2}{2}} d\xi_G'(j). \quad (18)$$

The top left of Fig. 3 shows, for sampling times $\Delta t = 1$ ms $< \tau_t$ and $\Delta t = 5$ ms $\sim \tau_t$, the cumulative displacement data and their residuals to the integrated Gaussian for all dust aggregates in the translation data set T1. It can be recognized that in both cases the displacement data follow a Gaussian distribution very closely (also see Fig. 16 in Appendix B for more sampling times). However, for values of $\Delta t \lesssim \tau_t$, the residuals are, on the order of a few percent, systematic and possess a characteristic quadruple-peaked shape, which suggests that a single Gaussian may not be the exact description for the one-dimension displacement. For $\Delta t \gtrsim \tau_t$, the residuals are randomly distributed with a standard deviation on the order of 1%.

A systematic deviation from a single Gaussian has been observed before and is usually described by an additional exponential function [19]. However, a combination of two Gauss functions has also been reported to fit the data [19]. We tried both approaches and found that a double-Gauss ansatz results in a better fit to the data. Details of these approaches are presented in Appendix B. From the best fit function, we

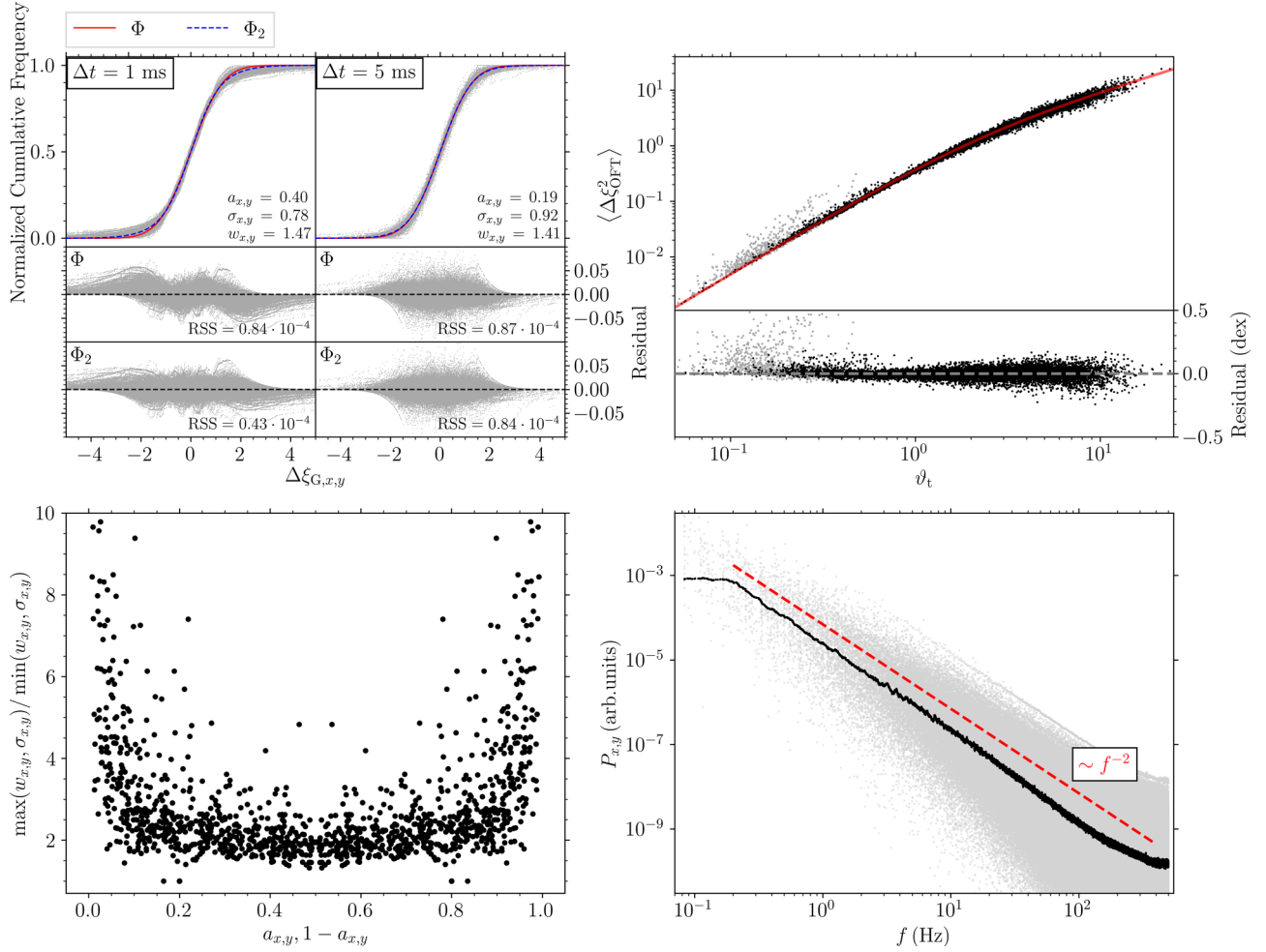


FIG. 3. Full characterization of the translational Brownian trajectories of all particles in data set T1. Top left: One-dimensional displacement data after normalization following Eq. (17). The solid red curves show the normalized error integrals [Eq. (18)]. Additionally, a double Gaussian fit to the composite data of all particles is shown (dashed blue curves). A fit must be used since Eq. (B1) cannot be normalized in the same way a singular Gaussian can. The residuals for the single and double Gaussians are shown in the second and third rows of the plots. The left and right panels were calculated for sampling times of $\Delta t = 1$ ms and $\Delta t = 5$ ms, respectively. Top right: $\langle \xi_{\text{OFT}}^2 \rangle$ values as a function of ϑ_t for the translational Brownian motion in x and y directions and comparison to Eq. (21) (red curve, color online). Data points that were discarded when fitting to single-particle data before normalization are shown in gray. The bottom panel shows the residuals in logarithmic units. Bottom left: Ratio of the width of the wider to the narrower Gauss function, $\frac{\max(\sigma_{x,y}, w_{x,y})}{\min(\sigma_{x,y}, w_{x,y})}$ for $\Delta t = 1$ ms, with $\sigma_{x,y}$ and $w_{x,y}$ from Eq. (B1), as a function of the amplitude ($a_{x,y}$ or $1 - a_{x,y}$, respectively) of both Gaussians. The width ratio for each set of amplitudes is identical. Bottom right: Spectral density distribution of the translational displacements at $\Delta t = 1$ ms in x and y , represented by the light gray dots, where $P_{x,y}$ is the signal strength and f the frequency, according to Eq. (29). A moving average with a window size equal to the number of particles is shown in black. The dashed line represents the f^{-2} slope, which is expected for Brownian motion.

determined the mean square displacement $\langle \Delta x^2 \rangle$ by assuming that this is the square of the standard deviation given by the 16% and 84% confidence level of the fit function, in analogy to the single-Gauss distribution function.

In the next step, the retrieved $\langle \Delta x^2 \rangle$ values were plotted as a function of Δt (see Fig. 13 in Appendix A for an example) and Eq. (1) was fitted to the data, which resulted in a set of four fit values for the masses m_x , m_y and the translational response times $\tau_{t,x}$, $\tau_{t,y}$ of each dust aggregate and for the two spatial directions x and y .

Figure 2 shows the corresponding data for all the particles and a comparison to the disturbance levels caused by the CMS control sequence (curved red band) and by the discretization

noise, shot noise, and brightness flickering of the illumination source (hatched bands, see legend). The various noise sources are discussed in Appendix F. The symbols are slightly offset to the right (left) for data set T1 (data set T2). Gray symbols were not used to fit Eq. (1). As can be seen, none of the particles in our data-set T2 are affected by the CMS operation and only very few in the larger data set T1.

The goodness with which the data of the complete ensemble of our particles follows the Ornstein-Fürth relation [Eq. (1)] can be assessed by rescaling

$$\langle \xi_{\text{OFT}}^2 \rangle = \frac{\langle \Delta x^2 \rangle}{2 \left(\frac{kT}{m} \right) \tau_t^2} \quad (19)$$

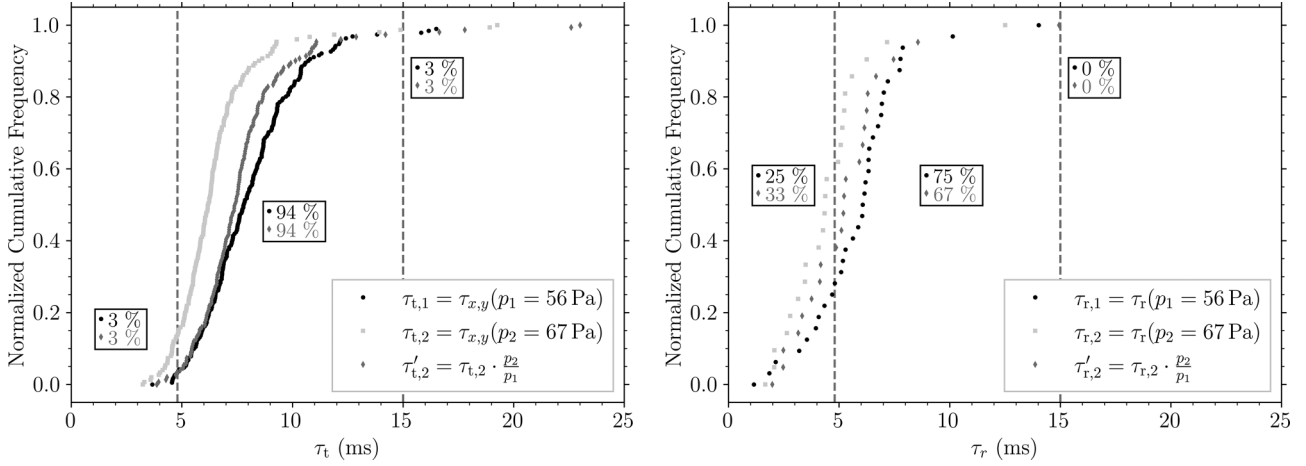


FIG. 4. The measured response times of the dust aggregates. Left: Cumulative histogram of the combined $\tau_{t,x}$ and $\tau_{t,y}$ values for the first injection at 56 Pa gas pressure (indicated by the black circles) and by the second injection at 67 Pa gas pressure (indicated by the gray squares). To get rid of the dependency of the response time on gas pressure (or density), as suggested by Eq. (22), the light gray diamonds show the second-injection data multiplied by the pressure ratio. The two vertical dashed lines correspond to $\tau_t = 4.8$ ms and $\tau_t = 15$ ms, respectively, which should be the lower and upper limits of the expected values (see Sec. IV A). The percentages of data points in the respective ranges are shown in the black boxes for the first and (adjusted) second injections. Right: Same for the rotational response times τ_r .

and

$$\vartheta_t = \frac{\Delta t}{\tau_t} \quad (20)$$

and using the fit values for m and τ_t for each particle and each spatial direction. Then, Eq. (1) transforms into a unique form

$$\langle \xi_{\text{OFT}}^2 \rangle = \vartheta_t - 1 + e^{-\vartheta_t}. \quad (21)$$

In the top right of Fig. 3, this function is plotted as a red curve and compared to the measured and rescaled data points in the x direction. The close relation between measured and theoretical values can be seen, with statistical deviations in the few percent range for $\vartheta_t \lesssim 1$ and on the order of 10% for $\vartheta_t \gtrsim 1$ (see bottom panel in the top right of Fig. 3). For $\vartheta_t < 1$, there are, besides the statistical deviations, also systematic deviations visible, which stem from the non-Gaussian behavior of the trajectory (see above). For the choice of the best fit for each particle, these systematic deviations were discarded (see Sec. IID).

Figure 4 (top) shows a combined cumulative histogram of the collective $\tau_{t,x}$ and $\tau_{t,y}$ data for the two dust injections, with ambient gas pressures of 56 Pa and 67 Pa, respectively. As the mean-free paths of the gas molecules for these pressures are ~ 170 μm and ~ 140 μm , respectively, and, thus, much larger than the particle dimensions (free-molecular flow regime), the gas-grain response time of the spherical monomer grains can be calculated by

$$\tau_t = \frac{\rho r_0}{\rho_g \bar{v}}, \quad (22)$$

with $\rho = 2000$ kg m^{-3} [20], ρ_g , $r_0 = (0.725 \pm 0.030)$ μm [13] and $\bar{v} = 477$ m s^{-1} being the bulk density of the monomer grains, the N_2 -gas density, the grain radii, and the mean speed of the N_2 molecules, respectively. With $\rho_g = 6.3 \times 10^{-4}$ kg m^{-3} for the first and $\rho_g = 7.5 \times 10^{-4}$ kg m^{-3} for the second dust injection, we get $\tau_t = 4.8$ ms and 4.1 ms, respectively. This is in good agreement with the smallest

occurring response-time values in Fig. 4 (top). In addition to the two measured response-time distribution functions, we also plotted the response-time distribution function of the second injection of the dust cloud, but rescaled to the lower gas density of the first dust injection. Although there are slight differences in the upper half of the response times that are possibly due to somewhat different large-aggregate morphologies, the agreement for response times similar to that of the monomer grains or small aggregates is good.

B. Analysis of the rotational Brownian motion

The analysis of the rotational Brownian motion of the dust aggregates was performed in complete analogy to the translational Brownian motion, as shown in Sec. III A. From the recorded tracks and the ellipse-fitting algorithm (see Fig. 11 in Appendix A for an example), the angular orientation θ_i of each particle was determined for all available time stamps $t_i = i \Delta t_0$, with $\Delta t_0 = 1$ ms and $i = 0, \dots, N$. We then derived the one-dimensional angular displacement data through

$$\Delta\theta(j) = \theta_{i+j} - \theta_i, \quad (23)$$

with

$$\Delta t(j) = j \Delta t_0 \quad (24)$$

and $j = 1, 2, 3, \dots; i = 0, j, 2j, \dots$. As in the case of translation, we derived one-dimensional angular displacement arrays with lengths $\sim \frac{N}{j}$. Also, all $\Delta\theta(j)$ should obey a Gaussian distribution. Thus, we also size-sorted the $\Delta\theta(j)$ values for each $\Delta t(j)$ from the smallest (negative) value (data point number 1) to the largest value (data point number $\sim \frac{N}{j}$) and again fitted error integrals [see Eq. (16)] to the normalized cumulative histograms with the two fit parameters $\sigma_\theta^2 \equiv \langle \Delta\theta(j)^2 \rangle$ and $\delta_\theta \equiv \langle \Delta\theta(j) \rangle$, respectively. The left of Fig. 16 in Appendix A shows as an example again particle 1 from Fig. 1 with its cumulative angular-displacement histograms for $\Delta t = 1, 5, 10, 21, 35, 50$ ms together with the

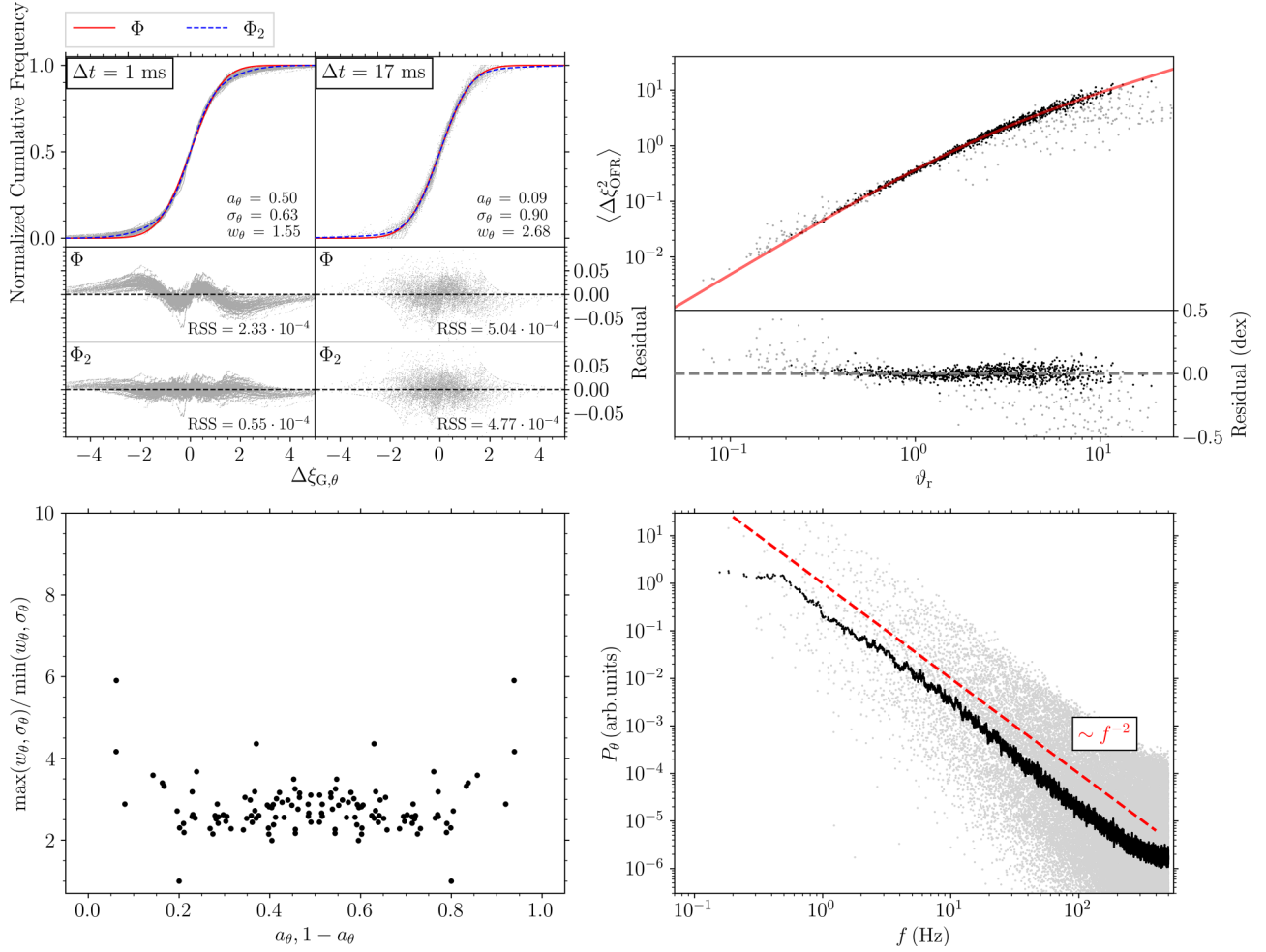


FIG. 5. Full characterization of the rotational Brownian trajectories of all particles in data set R1. Top left: Angular displacement data after normalization analogous to Eq. (17). The solid red curves show the normalized error integrals [analogous to Eq. (18)]. Additionally, a double Gaussian fit to the composite data of all particles is shown (dashed blue curves). A fit must be used since Eq. (B1) cannot be normalized in the same way a singular Gaussian can. The residuals for the single and double Gaussians are shown in the second and third rows of the plots. The left and right panels were calculated for sampling times of $\Delta t = 1$ ms and $\Delta t = 17$ ms, respectively. Top right: $\langle \xi_{\text{OFR}}^2 \rangle$ values as a function of ϑ_τ for the rotational Brownian motion and comparison to Eq. (27) (red curve, color online). Data points that were discarded when fitting to single-particle data before normalization are shown in gray. The bottom panel shows the residuals in logarithmic units. Bottom left: Ratio of the width of the wider to the narrower Gaussian function, $\frac{\max(\sigma_\theta, w_\theta)}{\min(\sigma_\theta, w_\theta)}$ for $\Delta t = 1$ ms, with σ_θ and w_θ from the rotational equivalent to Eq. (B1), as a function of the amplitude (a_θ or $1 - a_\theta$, respectively) of both Gaussians for all particles in data set R2. The width ratio for each set of amplitudes is identical. Bottom right: Spectral density distribution of the rotational displacements at $\Delta t = 1$ ms for every particle in data set R2, represented by the light gray dots, where P_θ is the signal strength and f the frequency, according to Eq. (30). A moving average with a window size equal to the number of particles is shown in black. The dashed line represents the f^{-2} slope, which is expected for Brownian motion.

best Gaussian-integral fits. Figures 5 and 16 show the same for all particles in data set R1 after normalization analogous to the translational case [see Eqs. (17) and (18)]. Similar to the translational case, the overall agreement with a Gaussian is good, but the systematic deviations are even more pronounced and lessen only at very high sampling times $\Delta t \gtrsim 17$ ms (see Fig. 5 and Fig. 16 in Appendix B).

As for the translational Brownian motion, in the next step the $\langle \Delta\theta(j)^2 \rangle$ values were plotted as a function of $\Delta t(j)$ (see Fig. 13 in Appendix A for an example) and fitted to Eq. (2), using the same algorithm as described for the translational Brownian motion (see Sec. III A). Figure 2 shows all particles in data sets R1 and R2. This resulted in values for the moment

of inertia I (data set R1) and the rotational response time τ_r (data set R2) of each dust aggregate.

As for the translational Brownian motion (see Sec. III A), the goodness with which the data of the complete ensemble of our particles follow the Ornstein-Fürth relation [Eq. (2)] can be assessed by rescaling

$$\langle \xi_{\text{OFR}}^2 \rangle = \frac{\langle \Delta\theta^2 \rangle}{2 \left(\frac{kT}{I} \right) \tau_r^2} \quad (25)$$

and

$$\vartheta_\tau = \frac{\Delta t}{\tau_r} \quad (26)$$

and using the fit values for I and τ_r for each particle. Then, Eq. (2) becomes

$$\langle \xi_{\text{OFR}}^2 \rangle = \vartheta_r - 1 + e^{-\vartheta_r}. \quad (27)$$

In the top right of Fig. 5, this function is plotted as a red curve and compared to the measured and rescaled data points. The close relation between measured and theoretical values can be seen, with statistical deviations in the few 10% range (see bottom panel in the top right of Fig. 5). As in the case of translational Brownian motion, systematic deviations from the expected curve can be seen for values $\vartheta_r < 1$, which are also caused by the non-Gaussian behavior of the rotational trajectory. For the choice of the best fit of each particle, these systematic deviations were also discarded (see Sec. IID). The deviations for values $\vartheta_r > 1$ stem from a lack in temporal resolution at large sampling times and were discarded by hand when fitting to the data, as discussed in Sec. IID.

For a comparison to the translational friction times of the aggregates, we also plotted in Fig. 4 (bottom) a cumulative histogram of the rotational response times. If we apply the same limits for τ_r as for τ_t (dashed vertical lines in Fig. 4), it is apparent that no particles exceed the upper limit, but a considerable fraction of all particles fall below the lower limit of τ_r .

IV. RESULTS AND DISCUSSION

Similar to the previous section, the results of the translational and the rotational motion analysis will be discussed separately. This is followed by a discussion about correlations between translational and rotational properties of dust aggregates and, finally, the derivation of the fractal dimension based on the observed agglomerates.

A. Translational Brownian motion

Translational Brownian motion analysis could be performed completely for 362 agglomerates (data set T1). Applying even tougher filter criteria left 172 agglomerates (data set T2) for which the analysis could be performed with the highest accuracy. An optical visualization of the two data sets is shown in Fig. 2.

1. Systematic deviations from Gaussian displacements

As demonstrated in Figs. 3 and 16, there are systematic deviations from a Gaussian distribution of the one-dimensional displacements for small sampling times $\Delta t \lesssim 5$ ms and all agglomerate masses, whereas for $\Delta t \gtrsim 5$ ms the deviations from Gaussian are random and mark the noise level down to which we can extract the data. To mathematically describe the systematic deviations, we fitted a double Gaussian as well as a combination of a Gaussian and an exponential function, as suggested by Wang *et al.* [19], to the data derived for each particle. It turned out that the double Gaussian fits the displacement data better than an additional exponential function (see Table II). Figure 17 in Appendix B demonstrates for which cases the fit quality can be improved. In the top left of Fig. 3, we show that the overall improvement by fitting the sum of two Gaussians cannot only be measured quantitatively but also leads to the complete disappearance of

TABLE II. Comparison of the residual sums of squares, RSS_t for translation and RSS_r for rotation, respectively (following the traditional definition but normalized by the number of data points), of the three different methods of fitting to the displacement data, namely, the single-Gauss function [Eq. (16)], double-Gauss function [Eq. (B1)], and the sum of a Gaussian and an exponential function [Eq. (B2)]. The values shown are the medians across all particles at $\Delta t = 1$ ms from data set T1 for both spatial displacements and data set R1 for angular displacements, respectively. The reference to data sets T1 and R1 can be found in Fig. 23 in Appendix G.

	Single Gaussian	Double Gaussian	Gaussian + Exp.
$\langle \text{RSS}_t \rangle$	8.2×10^{-5}	2.7×10^{-5}	6.6×10^{-5}
$\langle \text{RSS}_r \rangle$	21.1×10^{-5}	3.1×10^{-5}	4.4×10^{-5}

the quadruple-peaked residuals for $\Delta t = 1$ ms. It might seem surprising that a unique second Gaussian can be found for the normalized data, but looking at the top left panel of Fig. 17 in Appendix B shows that this could be expected because the highest improvements in fit quality (highest values of $\frac{\text{RSS}_{\text{single}}}{\text{RSS}_{\text{double}}}$) are closely grouped around a width ratio of the two Gaussians of ~ 2 . This is confirmed by the data in the bottom left of Fig. 3, where we plotted the ratio of the width of the wider to the narrower Gauss function, $\frac{\max(\sigma_{x,y}, w_{x,y})}{\min(\sigma_{x,y}, w_{x,y})}$, with $\sigma_{x,y}$ and $w_{x,y}$ from Eq. (B1), as a function of the amplitude ($a_{x,y}$ or $1 - a_{x,y}$, respectively) of both Gaussians. The width ratio for each set of amplitudes is therefore identical. It can be seen that the width ratio is symmetric to $a_{x,y} = 0.5$ and groups around values of $\frac{\max(\sigma_{x,y}, w_{x,y})}{\min(\sigma_{x,y}, w_{x,y})} = 2$ for $0.2 \lesssim a \lesssim 0.8$. For amplitude values outside this range, the width ratio can obtain higher values. However, due to the smallness of the amplitude of one of the two Gaussians in these cases, the width ratios can only be derived with large error margins, so we conclude that

$$\frac{\max(\sigma_{x,y}, w_{x,y})}{\min(\sigma_{x,y}, w_{x,y})} = 2 \quad (28)$$

could be valid for all amplitudes. As for the amplitudes themselves, there is no obvious grouping present, but all values occur equally often.

We can not identify any noise source in our data that can quantitatively explain this behavior. In Appendix F, we list the investigated noise effects, which are partly also displayed in Fig. 2.

Next we compare the power spectrum of the one-dimensional trajectories $x(t)$,

$$P_x(f, T) = \frac{1}{T} \left| \int_0^T x(t) e^{-i2\pi ft} dt \right|^2, \quad (29)$$

with the expectation for pure (single-)Gaussian Brownian motion. Here, f and T are the frequency and the total observation time of the trajectory, respectively. In the ideal case of infinitely long observation time, $T \rightarrow \infty$, the power spectrum of the Brownian diffusion follows a f^{-2} power law for all frequencies; for finite observation times T , however, there is a cutoff at a frequency of $f \approx 1/T$ [21].

The power spectrum for our standard particle (particle 1 in Fig. 1) is shown in Fig. 15 in Appendix A (top for

translational, bottom for rotational Brownian motion). The data nicely show the f^{-2} behavior over most of the frequency range, with a slight indication of flattening at high frequencies.

The bottom right plot in Fig. 3 shows the power spectrum for all particles in data set T2 (gray data points). The black data points mark a moving geometric average of these data with a window size equal to the number of particles.

We can recognize the f^{-2} power law for frequencies $f \lesssim 200$ Hz and a flatter slope for $f \gtrsim 200$ Hz. It is remarkable that the frequency at which the f^{-2} power law ends equals a timescale of $\tau \approx 5$ ms, which is close to the characteristic translational friction time of the particles. Thus, the power spectrum also shows that a transition from pure Gaussian (f^{-2}) Brownian motion to something more complex occurs at sampling times below the gas-grain coupling (or dissipation) time, i.e., in the ballistic limit of Brownian motion in which the time-averaged equivalence between fluctuation and dissipation is not necessarily fulfilled.

2. Absolute values of the translational friction times and their correlation with aggregate mass

Fractal aggregates (see Sec. IV C) should possess response times that are, in general, larger than those of their constituent monomer grains due to partial shielding of some monomer grains from the gas-flow field. However, this effect might be rather small for very low fractal dimensions due to the openness of the corresponding aggregate structures. Mukai *et al.* [22] simulated the two cases of BPCA (ballistic particle-cluster aggregation, $d_f \approx 3$) and BCCA (ballistic cluster-cluster aggregation, $d_f \approx 1.9$) and found for the latter a relation between mass m (or number of constituent grains) and the average projected geometric cross section A of the form $A \propto m^{0.95}$, from which a mass dependency of the response time of $\tau_t \propto \frac{m}{A} \propto m^{0.05}$ can be derived in the free-molecular-flow limit. For BCCA aggregates with constituent-grain numbers between $N = 1$ and $N = 1000$ (this is approximately the range of aggregate masses in our study; see Fig. 18 in Appendix C), the increase of the ratio between mass and geometric cross section, a proxy for the response time, is about a factor of 3. Thus, we would not expect response times above $\tau_t \approx 15$ ms, which is true for the bulk of the data points in Fig. 4 (top). Following the simulations of Mukai *et al.* [22] and suggesting that our aggregates have a low fractal dimension too (see Sec. IV B), we expect a slight positive correlation between τ_t and m . This behavior can be recognized in Fig. 6 where τ_t is plotted as a function of m for all particles of data set T2. A formal power-law fit to the displayed data yields a slope of 0.04 ± 0.02 , which is in good agreement with the expectation.

B. Rotational Brownian motion

Rotational Brownian motion analysis could be performed completely for 65 agglomerates (data set R1). Applying even tougher filter criteria left 55 agglomerates (data set R2) for which the analysis could be performed with the highest accuracy. An optical visualization of data set R1 is shown in Fig. 2.

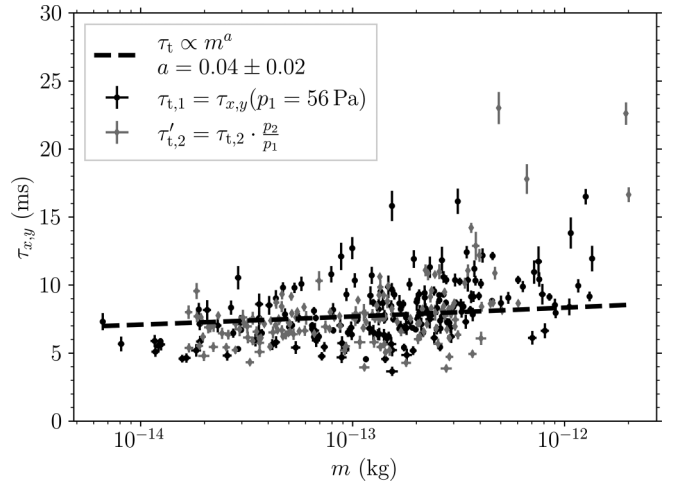


FIG. 6. The masses and translational response times of all dust aggregates from data set T2. For the dust aggregates of the second injection, the response times were multiplied by the pressure ratio of the two injections to account for the higher gas pressure and, thus, systematically smaller friction times after the second injection. The dashed line shows the best-fitting power-law function with a slope of 0.04 ± 0.02 and corresponds well to the predictions by Mukai *et al.* [22] for BCCA particles.

1. Systematic deviations from Gaussian displacements

As in the case of translational Brownian motion (see Sec. IV A), we also observed in the rotational case systematic deviations from a Gaussian distribution for the angular displacement data $\Delta\theta$ for short sampling times Δt . In Fig. 5, we compile the full characterization of the rotational data set R2, equivalent to the translational case shown in Fig. 3. The top left of Fig. 5 shows that the double-Gaussian leads to a much better fit of the overall displacement data than the single Gaussian [analogous to Eq. (18)] also for the full ensemble of particles. The top right of Fig. 5 displays the two best-fitting Gaussians in direct comparison. The bottom left of Fig. 5 emphasizes that the width ratio of the two Gaussians is close to 2, as in the translational case. Finally, the bottom right of Fig. 5 shows the power spectrum of the rotational trajectories $\theta(t)$,

$$P_\theta(f, T) = \frac{1}{T} \left| \int_0^T \theta(t) e^{-i2\pi ft} dt \right|^2, \quad (30)$$

with the sampling time T and the frequency f . Similar to the translational case, we can distinguish between three frequency ranges. For small frequencies, $f \lesssim 1$ Hz, the power spectrum is rather flat. For intermediate frequencies, $1 \text{ Hz} \lesssim f \lesssim 200$ Hz, the spectrum follows a power law, with a slope close to -2 . For high frequencies, $f \gtrsim 200$ Hz, the spectrum again becomes flatter. We interpret this behavior in the same way as for translational Brownian motion (see Sec. IV A).

2. Absolute values of the rotational friction times and their correlation with the moment of inertia of the dust aggregates

In Fig. 4 (bottom), we plotted a cumulative histogram of all values of τ_r . Different to the translational case, the gas-grain response times for rotation do not entirely fall into the

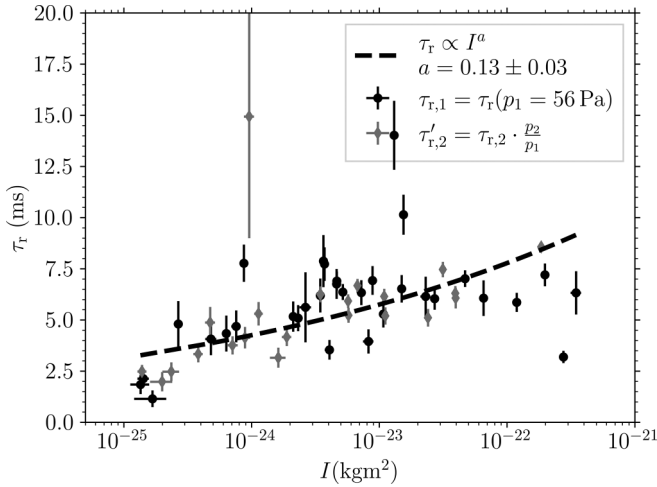


FIG. 7. The moments of inertia and rotational response times of all dust aggregates from data set R2. For the dust aggregates of the second injection, the response times were multiplied by the pressure ratio of the two injections to account for the higher gas pressure and, thus, the shorter friction time after the second injection. The dashed line shows the best-fitting power law function with a slope of 0.13 ± 0.03 .

predicted range of values between $\tau_t = 4.8$ ms and $\tau_t = 15$ ms, but 25–33% of the data fall below $\tau_t = 4.8$ ms, with no particle above $\tau_t = 15$ ms. The reason for this unexpected behavior is unclear.

It is certainly interesting to see whether a correlation between the moment of inertia and the rotational friction time exists. Lacking numerical data about this, there is, however, no model available to compare these data too. In Fig. 7, we show a plot of the rotational friction times as a function of the moment of inertia for all particles from data set R2. Based upon the relation between translational response time and mass, we tried to fit a power law of the form $\tau_r \propto I^a$ and derived a slope of $a = 0.13 \pm 0.03$ (see Fig. 7).

3. Deviations from the Ornstein-Fürth theory for large values of Δt

As can be seen in the uppermost curves in Fig. 2, the measured data seem to deviate from the Ornstein-Fürth relation for large values of $\langle \Delta\theta^2 \rangle$. In contrast to the translational Brownian motion, for which the displacement Δx increases beyond bonds for $\Delta t \rightarrow \infty$, the Brownian rotation angle is periodic and limited to a range $\theta = [-\pi/2 \text{ rad}, \pi/2 \text{ rad}]$. This is observationally manifested by the onset of a saturation of the $\langle \Delta\theta^2 \rangle$ data for large values of θ_t in Fig. 2.

C. Combining translational and rotational Brownian motion and the derivation of the fractal dimension of the agglomerates

After the derivation of the properties of the dust aggregates through Brownian translational and rotational motion, we here will try to compare the two friction times as well as to use the combined information of the particle masses and moments of inertia to derive the fractal dimension of the ensemble of dust aggregates.

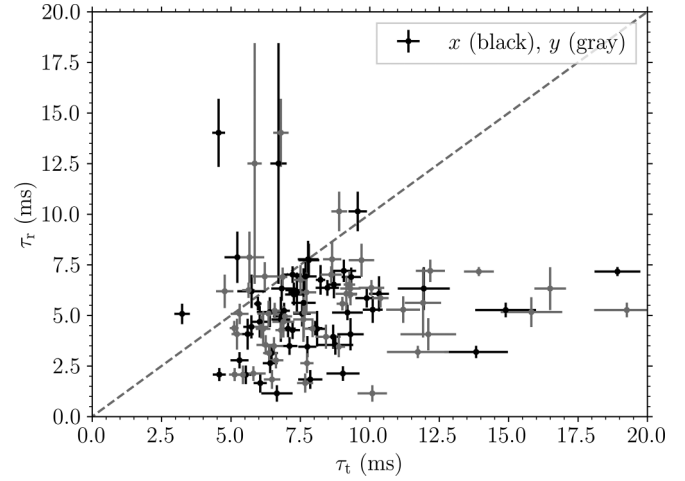


FIG. 8. The translational and rotational response times, τ_t and τ_r , respectively, for all particles in data set R2. The dashed diagonal line shows the expected relation $\tau_t = \tau_r$.

1. Comparison of the friction times derived through translational and rotational Brownian motion

In the previous subsections, we discussed the individual distribution of the translational and rotational friction times (see Fig. 4). In Fig. 8, we now display the relation between τ_t and τ_r . A clear deviation from $\tau_t = \tau_r$ (dashed line in Fig. 8) can be seen. This is unexpected, because each mass element dm in the dust aggregate (e.g., a monomer grain), interacting with the ambient gas, characterized by the respective response time, should experience a force $dF = dm v/\tau_t$ as well as a torque $dD = dI \omega/\tau_r$, with v and ω being the relative translational speed and rotational angular frequency between dust aggregate and gas, the latter assumed to be at rest. Due to $dI = dm r^2$ and $v = \omega r$, with r being the distance of the mass element from the rotation axis of the aggregate, we get $\tau_t = \tau_r$. If the deviation from this equality seen in Fig. 8 is real, the effect can only be caused by a collective action of all mass elements, which then obviously shields particles better from the frictional interaction with the ambient gas in the translational than in the rotational motion, hence often $\tau_t > \tau_r$. However, we cannot exclude that the systematic deviation between the two response times is caused by noise in the data, particularly those cases for which $\tau_r < 5$ ms, i.e., when the response time of the dust aggregate is even shorter than that of a monomer grain.

2. Derivation of the fractal dimension of the dust aggregates

For small collision speeds and microscopic particles, each collision results in a so-called hit-and-stick event. This means that the colliding grains establish a stiff connection at the first point of contact. This scenario has been reproduced in models [23] as well as in laboratory experiments [24]. Thus, the resulting agglomerates are not compact and grains at the periphery may shield incoming particles from reaching the interior. Depending on the mass-frequency distribution of the aggregates at any given time and the importance of aggregate rotation, this may result in aggregate structures with fractal dimensions [see Eq. (12)] in the range $d_f = 1 \dots 3$.

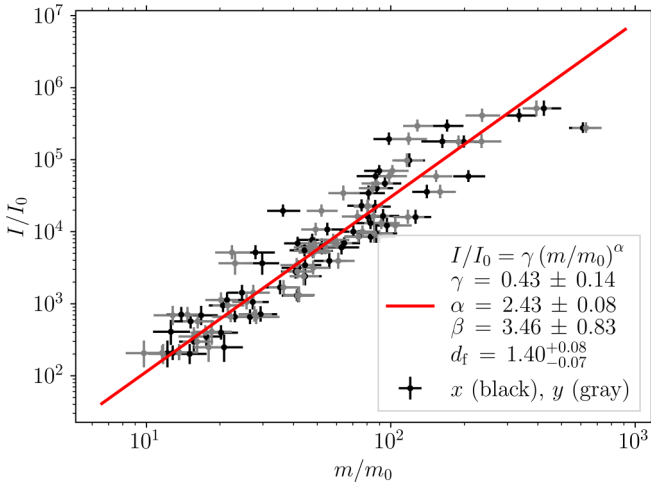


FIG. 9. The moment of inertia of the dust agglomerates in data set R2, determined by the rotational Brownian motion analysis, as a function of the mass of the agglomerates, determined by the translational Brownian motion analysis. A power-law fit is shown by the red line. Its slope provides the ensemble fractal dimension of $d_f = 1.40$. The black data points with errors were derived from the Brownian motion in x direction, the gray data points with errors from the y direction. The moments of inertia for both mass values are identical.

Particles with $d_f = 1$ are stringlike agglomerates, whereas those with $d_f = 3$ are porous clusters with a constant, i.e., mass-independent, density.

Using Eqs. (11) and (12), we get a relation between the moment of inertia I and the mass m of an agglomerate with a fractal dimension d_f , which reads

$$I \propto m^{(1 + \frac{2}{d_f})}. \quad (31)$$

Thus, the slope α in a log-log plot of I versus m of an ensemble of dust aggregates is given by $\alpha = 1 + 2/d_f$ and we finally get the fractal dimension of the ensemble of dust aggregates through

$$d_f = \frac{2}{\alpha - 1}. \quad (32)$$

Fitting a power law to the data shown in Fig. 9, according to Eq. (31), yields $d_f = 1.40^{+0.08}_{-0.07}$. This is a remarkably low value for the fractal dimension and suggests that the rotational motion has a considerable influence on the outcome of a collision. Paszun and Dominik [25] studied the influence of the gas density for Brownian-motion-induced agglomeration and found that the fractal dimensions fall into the range $d_f = 1 \dots 1.46$. For high gas densities, Brownian motion is in the diffusive limit so two dust aggregates cannot penetrate deep into one another so the lowest fractal dimensions result. For low gas densities, both the translational and rotational Brownian motion are ballistic so a slight chance exists that some interpenetration can occur. Thus, the fractal dimension in this case reaches the highest value of $d_f = 1.46$ possible for Brownian motion. The model by Paszun and Dominik [25] can explain previous results on Brownian-motion driven fractal agglomeration, which showed that $d_f \approx 1.4$ [7].

Here, we do not claim that the agglomerates in ICAPS were entirely formed by Brownian motion because we have

indications that the initial growth was also affected by grain charging. We will describe this in more detail in a forthcoming paper. However, the low fractal dimension found in this work is a clear indication that hit-and-stick processes were at work.

It should be emphasized that the ensemble fractal dimension derived by the analysis of the translational and rotational ballistic Brownian motion is independent of any model assumption and relies entirely on Eq. (12), with the mass and the moment of inertia as direct outputs from the motion analysis of the aggregates.

V. LIMITATIONS

Any analytical procedure is limited by the quality of the available data, statistical uncertainties of measurement, and other biases. The method we present for mass and friction time determination using the Ornstein-Fürth equation is particularly sensitive to biases caused by noisy data but also has other limitations, which we will briefly discuss in the following.

First, small inaccuracies can creep in during data preparation due to tracking. However, we tried to minimize these as far as possible. For example, a subpixel accuracy algorithm was implemented to determine the center of the particles. But even this only improves the tracking accuracy and does not fully guarantee that the correct center was determined. Furthermore, a flat-field correction was implemented to improve tracking. However, this value is very sensitive, especially for small particles, because possibly darker edge pixels of a particle can be detected as background and thus the determination of the position of the center of mass of the particle might be erroneous.

Unlike the mass, the moment of inertia and the two response times τ_t and τ_r are nonunique for aggregates and depend on the orientation of the grains with respect to the momentary velocity vector in translation and rotation. Although the expected range of variation should not exceed a factor of a few, due to the isotropy of Brownian motion, these ambiguities might affect the ensemble fractal dimension in an unknown way. It should also be noted that the determination of Brownian rotation, the orientation angles had to be measured. Besides harsh sharpness criteria, our ellipse-fitting routine required a certain amount of elongation of the dust aggregates. This not only led to much fewer dust aggregates in the rotational data set (65 particles in R1 versus 362 particles in T1, see Fig. 23) but might also have imposed selection effects with unknown consequences for the determination of the fractal dimension.

We tried to identify noise effects that could lead to misinterpretations of the measured particle trajectories and found that the corresponding noise levels are very small (see Appendix F). However, there might be undiscovered disturbances during the rocket flight that might also affect the results. One such effect might be the high mass loading of the particle samples investigated in this paper. As shown in Sec. II, the overall mass density of the grains exceeds the gas density by a factor 15–30. This leads to the situation that the mean-free path of the gas molecules (170 μm for the first dust injection) is on the same order as the mean distance between the dust particles ($\sim 50 - 500 \mu\text{m}$, depending on the aggregate mass). Thus, a proper thermalization of the gas between collisions

with nearby particles is not guaranteed. However, this effect might be very small and restricted to ultrashort timescales because the mean diffusion length of the gas molecules for the shortest timescale of $\Delta t = 1$ ms is ~ 9 mm and thus much larger than the other relevant length scales.

VI. CONCLUSIONS

With a unique experimental setup (see Sec. II), we were capable of studying the thermal motion of microscopic particles under microgravity conditions at high spatial and temporal resolution for extended periods of time. In this paper, we presented the acquired data of the translational and rotational Brownian motion of dust aggregates from the ballistic to the diffusive limit in rarefied gas (Knudsen number $\text{Kn} = 140 - 168$ with respect to the monomer-grain radius). Our data analysis shows that the particles follow the Ornstein-Fürth relation [Eq. (2)] closely (see the top right in Figs. 3 and 5), which allowed us to determine the four individual characteristic physical properties of a large number of dust agglomerates, namely, their mass and their moment of inertia as well as their translational and rotational response times. The high mass loading of the rarefied gas (density ratio between solids and gas $\sim 15 - 30$, see Sec. II) obviously has no effect on the Brownian motion of individual particles. We observed slight deviations from the one-dimensional Gaussian displacement behavior in the ballistic limit, which we cannot attribute to any possible noise source.

The translational friction falls into the expected range of values $\tau_t = 4.8 - 15$ ms, which can be determined by applying Eq. (22), valid for the free-molecular flow regime. A surprising and somewhat unexpected result is that the rotational response times of the dust aggregates seem to be on average slightly smaller than their translational counterparts (see Fig. 8). It still needs to be explained whether this finding is real or an artifact of the data analysis.

The mass determination of the dust aggregates can be performed in the ballistic limit, i.e., for all $\Delta t < \tau_t$, because it then follows Eq. (3), which only has the mass of an agglomerate as a free parameter, which is a unique property. The relative error of the mass determination is approximately $\pm \sim 0.1$ over the entire mass range (see Fig. 18 in Appendix C). Nonunique are the moment of inertia, which can equivalently be determined in the ballistic limit of the Brownian rotational motion [see Eq. (4)] and the two friction times. For the determination of the latter, the diffusive limits of the Brownian translational and rotational motion have additionally to be covered.

The relation between the moment of inertia and the mass of an ensemble of dust aggregates is determined by the fractal dimension, which is a characteristic property of the underlying growth process [9]. Figure 9 shows that Eq. (12) is well adopted by the ICAPS dust-aggregate ensemble and allowed us to determine, according to Eqs. (31) and (32), the fractal dimension to be $d_f = 1.40^{+0.08}_{-0.07}$.

This paper shows that a proper high-resolution Brownian motion analysis allows us to determine all basic properties of dust particles. In our future work, we plan to study Brownian motion for a wide range of particle sizes, materials, and shapes

and to correlate the fractal dimension of an ensemble of dust aggregates to the underlying growth process.

ACKNOWLEDGMENTS

This work was part of the ICAPS mission, which was supported by the German Space Agency (DLR) under Grants No. 50WM0336, No. 50WM0636, No. 50WM0936, No. 50WM1236, No. 50WM1536, No. 50WM1846, and No. 50WM2146. and the European Space Agency (ESA) through their SciSpacE program for this project and the Texus-56 Sounding Rocket flight. We also kindly acknowledge the support by the Belgian Science Policy Office (belspo) and the European Space Agency PRODEX Programme. We wish to thank Mark Bentley for kindly allowing us to use his particle growth simulation code [26].

The data underlying this paper will be shared on reasonable request to the corresponding author.

APPENDIX A: SINGLE-TRAJECTORY ANALYSIS OF PARTICLE 1 IN FIG. 1

In this Appendix, we exemplify the analysis of the single-particle translational and rotational trajectories by showing the results for particle 1 in Fig. 1. The properties of this particular dust aggregate are shown in Table I. Figure 10 displays the two-dimensional trajectory of the particle across its observation time of ~ 7 s and how it rotated during a segment of the trajectory, amounting to ~ 2 s, in which the particle was sharp enough to enable orientation measurements. Figure 11 shows snapshots of the particle with the fitted ellipses, used to derive its orientation, drawn on top. Figure 12 shows the size-sorted one-dimensional translational and rotational displacements of the particle. Figure 13 shows the one-dimensional spacial and angular mean square displacements of the particle as a function of the sampling time, together with the best-fitting function following Eq. (1) in the translational and Eq. (2) in the rotational case, respectively, which yielded the mass, moment of inertia and the translational and rotational friction times of the particle (see Table I). Figure 14 shows how the fit of a double-Gaussian, according to Eq. (B1), improves the representation of the displacement data in translation and rotation. Finally, Fig. 15 shows the spectral density distribution of the trajectory of particle 1 in translation and rotation.

APPENDIX B: ALTERNATIVES TO PURE GAUSSIAN DISPLACEMENT

Based on the kind of systematic deviations seen in Figs. 3 and 16, we tried, as an alternative to Eq. (16), to empirically improve the representation of the one-dimensional displacement data of the individual particle trajectories by two additional mathematical descriptions.

(I) The sum of two Gaussians,

$$\begin{aligned} \Phi_2(\Delta x(j)) = & \frac{1 - a_x(j)}{\sqrt{2\pi\sigma_x^2(j)}} \int_{-\infty}^{\Delta x(j)} e^{-\frac{(\Delta x'(j) - \delta_x(j))^2}{2\sigma_x(j)^2}} d\Delta x'(j) \\ & + \frac{a_x(j)}{\sqrt{2\pi w_x^2(j)}} \int_{-\infty}^{\Delta x(j)} e^{-\frac{(\Delta x'(j) - \delta_x(j))^2}{2w_x(j)^2}} d\Delta x'(j), \end{aligned} \quad (\text{B1})$$

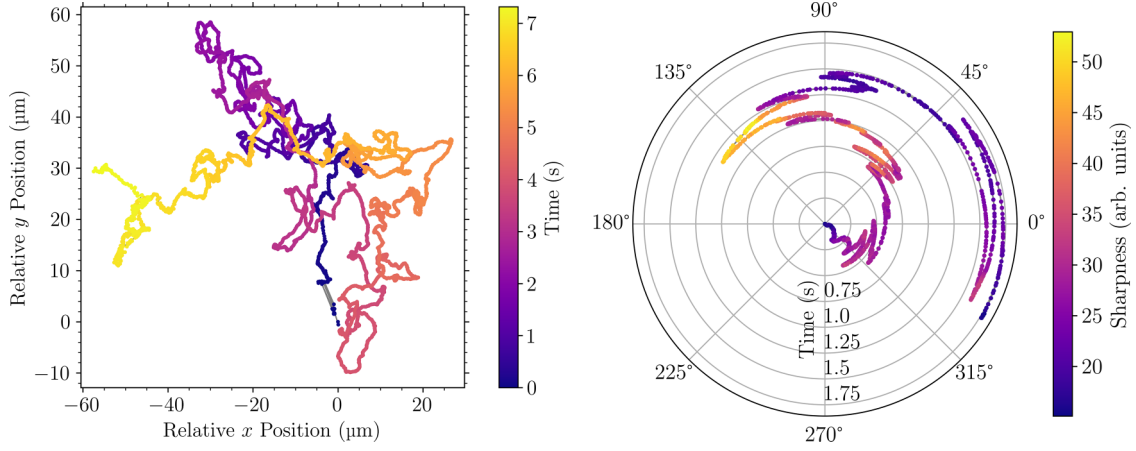


FIG. 10. Left: Track of particle 1 from Fig. 1. Each dot represents one time step of 1 ms with some larger gaps at the beginning of the track. The temporal evolution is shown through a color gradient from blue over red to yellow, and the dots are connected by a gray line in that order. Right: Orientation track of the same particle, shown as a polar plot with time on the radial axis. The sharpness of the cropped particle images, as described in Sec. II D, is represented in the color of the dots on an arbitrary scale from blue over red to yellow. Supplemental Material movies of the translational and rotational Brownian motion of this particle are also provided [27].

with $w_x(j)$ and $a_x(j)$ being the width and amplitude of the second Gaussian, respectively. The other parameters have the same meaning as in Eq. (16).

(II) The sum of a Gaussian and an exponential function,

$$\begin{aligned} \Phi'_2(\Delta x(j)) = & \frac{1 - a_x(j)}{\sqrt{2\pi\sigma_x^2(j)}} \int_{-\infty}^{\Delta x(j)} e^{-\frac{(\Delta x'(j) - \delta_x(j))^2}{2\sigma_x(j)^2}} d\Delta x'(j) \\ & + \frac{a_x(j)}{2\lambda_x(j)} \int_{-\infty}^{\Delta x(j)} e^{-\frac{|\Delta x'(j) - \delta_x(j)|}{\lambda_x(j)}} d\Delta x'(j), \end{aligned} \quad (\text{B2})$$

with $\lambda_x(j)$ being the width of the exponential function. Fitting both equations to our data sets showed that the sum of two Gaussians [Eq. (B1)] can represent the data much

better than the combination of a Gaussian with an exponential function (see Table II). The overall improvement of the fit quality by using the double-Gaussian recipe can be seen in Fig. 14 in Appendix A for particle 1 in Fig. 1. The tails at larger displacements are better represented by the double-Gauss fit, but still the fit is not perfect. However, for the purpose of determining the mean square displacement $\langle x^2 \rangle$, the actual choice of a single-Gauss or a double-Gauss fit is almost irrelevant (see vertical dash-dotted lines in Fig. 14 in Appendix A).

As shown in Fig. 16, the need for a correction to the single-Gauss solution decreases with increasing Δt . This can also be seen in Fig. 17, in which the width ratio of the two Gauss functions in the double-Gauss fit (top row) and the amplitudes of the two Gauss functions (middle row) are plotted as a function of the improvement of the fit quality, expressed by the ratio of the squared deviations in both cases, $\frac{\text{RSS}_{\text{single}}}{\text{RSS}_{\text{double}}}$, respectively. The bottom row additionally shows the width ratio of the two Gauss functions as a function of the amplitude of both Gauss functions. The tendency of the data to concentrate at smaller values of $\frac{\text{RSS}_{\text{single}}}{\text{RSS}_{\text{double}}}$ with increasing Δt can be easily seen when comparing the left, middle, and right columns of plots in Fig. 19. Thus, a considerable improvement of the fit quality by introducing a second Gaussian can only be achieved for small values of Δt , but in these cases the improvement can be up to a factor ~ 30 . As can be seen in the top left panel of Fig. 19, the highest improvement in fit quality corresponds to a width ratio of the two Gaussians of ~ 2 . In these cases, the amplitudes of the two Gauss functions are not constrained (left column, middle panel). This can also be seen in the bottom row of Fig. 19 where the width ratio of the two Gauss functions is shown as a function of their amplitudes. For higher width ratios, however, the amplitudes group around values close to 0 and 1. This suggests that the formal double-Gauss solutions are very close to the single-Gauss case.

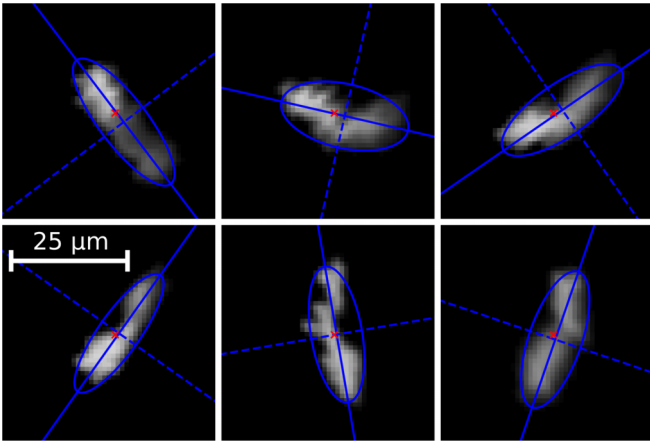


FIG. 11. Snapshots of the orientation of particle 1 from Fig. 1. The ellipse fitted to its contour is shown in blue, as well as the orientation of the semimajor (solid line) and semiminor (dashed line) axis, respectively. The center of light extinction is denoted with a red cross in each image.

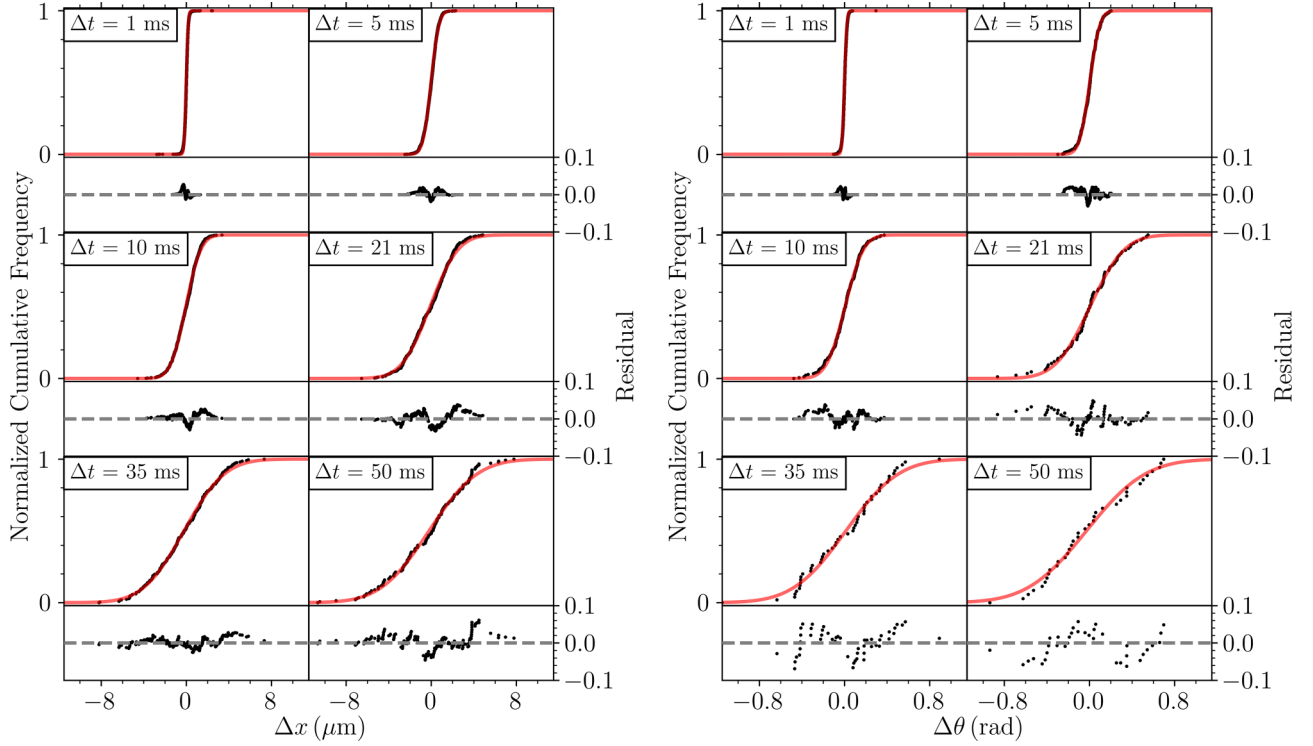


FIG. 12. Left: Examples of the size-sorted $\Delta x(j)$ data for particle 1 in Fig. 1 from the trajectory displayed on the left of Fig. 10 for time increments of $\Delta t = 1, 5, 10, 21, 35, 50$ ms (data points). The solid curves show the best-fitting error integrals [Eq. (16)] from which the values σ_x^2 and δ_x were derived. The plots at the bottom of each panel show the residuals between the measurements and Eq. (16). Right: The equivalent for the rotational case, showing the same data as displayed on the right of Fig. 10 and yielding σ_θ^2 and δ_θ from the fits [analogous to Eq. (16)].

We then applied again both replacements for the rotational equivalent of Eq. (16).

(I) The sum of two Gaussians, with $w_\theta(j)$ and $a_\theta(j)$ being the width and amplitude of the second Gaussian, respectively.

(II) The sum of a Gaussian and an exponential function, with $\lambda_\theta(j)$ being the width of the exponential function.

APPENDIX C: ACCURACY AND ISOTROPY OF THE MASS AND FRICTION TIME DETERMINATIONS

From the two physical quantities that can be derived from the one-dimensional Brownian displacement data, namely, the mass and the friction time of the particle, only the mass is

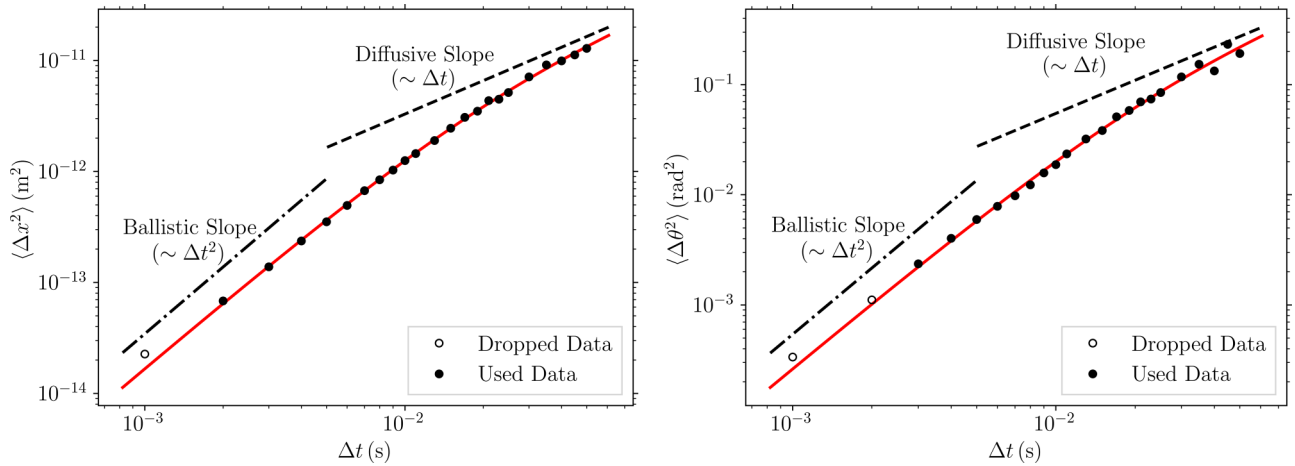


FIG. 13. Left: $\langle \Delta x(j)^2 \rangle$ values as a function of $\Delta t(j)$ (open and filled circles) for particle 1 in Fig. 1. The best fit function following Eq. (1) is shown as a solid red curve. As the data are one-dimensional displacements in the x direction, the fit procedure yields the mass $m_x = 2.4 \times 10^{-13}$ kg and the translational friction time $\tau_{t,x} = 9.6$ ms of the particle. The data points that were used in the fit are denoted by the filled symbols. The dash-dotted line denotes the slope of a perfect ballistic trajectory [Eq. (3)], whereas the dashed line shows the diffusive limit (slope and absolute value) of that particular particle [Eq. (7)]. Right: The equivalent for the rotational case. The best fit to Eq. (2) yields the moment of inertia $I = 1.5 \times 10^{-23}$ kg m² and the rotational friction time $\tau_r = 10.1$ ms of this particle.

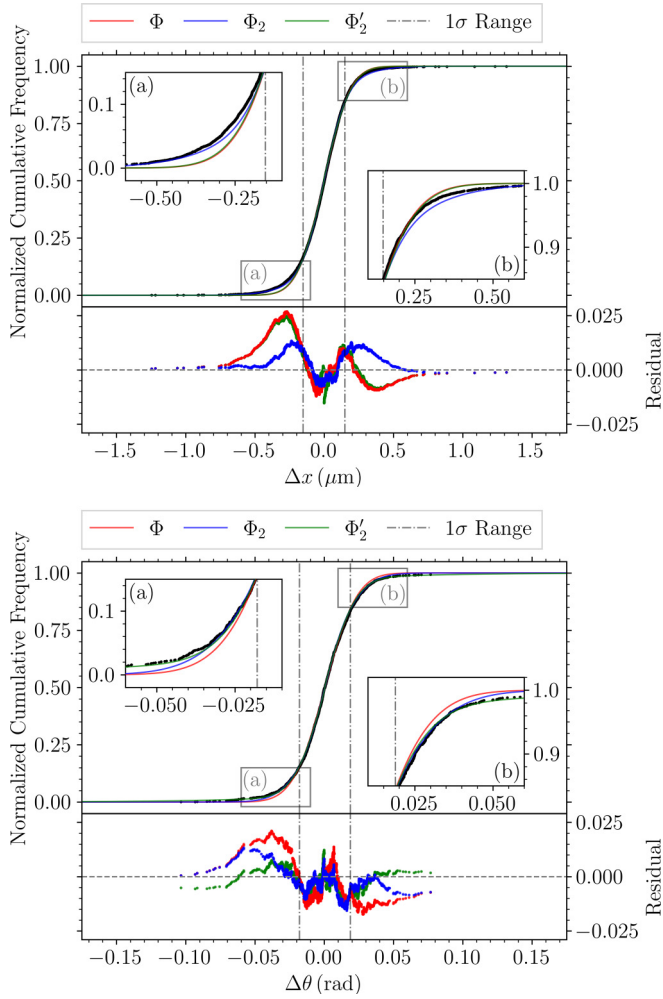


FIG. 14. Size-sorted $\Delta x(j)$ (top) and $\Delta \theta(j)$ (bottom) data for particle 1 from Fig. 1 for $\Delta t = 1$ ms. The solid curves show the best-fitting integrals, both for the single Gauss function [Eq. (16)], the sum of two Gauss functions [Eq. (B1)], and the sum of a Gaussian and an exponential function [Eq. (B2)]. The bottom segment of each plot shows the corresponding residuals between the measurements and the respective fit values. The dash-dotted lines mark the displacement values corresponding to the 1σ range boundaries.

a unique property that does not depend on the orientation of the aggregate relative to its direction of motion. The friction time, on the other hand, is actually a tensor with three (possibly different) eigenvalues. For dust aggregates with low fractal dimensions, $D_f \lesssim 2$, the ratio of the one-dimensional radii of gyration for two perpendicular spatial directions has been shown to obtain maximum values of ~ 2 [28]. Thus, the friction time might also vary by about that much from one spatial direction to the other (if Brownian rotation can be neglected) or as a function of time (if Brownian rotation is effective) in a single spatial direction. However, if we compare the scatter of the mass and friction time data in both spatial directions by evaluating $(m_x - m_y)/(m_x + m_y)$ and $(\tau_x - \tau_y)/(\tau_x + \tau_y)$, respectively, their distributions are indistinguishable (see Fig. 18, top right for mass and bottom right for friction time). It should be noted that the data sets for the mass (data set T1) and the friction time (data set T2)

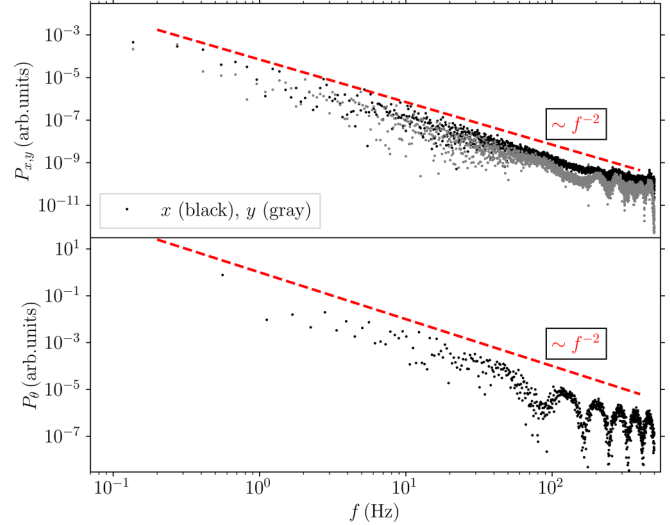


FIG. 15. Spectral density distribution of the Brownian trajectories of particle 1 in Fig. 1 and comparison to the expected slope of -2 (dashed lines, color online). Top: Translational Brownian motion for both spatial directions, x (black dots) and y (gray dots). Bottom: Rotational Brownian motion.

are different (see Fig. 23 in Appendix G), but the criteria for the goodness of the Ornstein-Fürth fits were the same, namely, $\Delta m/m \leq 0.1$ and $\Delta \tau_i/\tau_i \leq 0.1$, for each spatial direction independently. The FWHM of both histograms in Fig. 18 is ± 0.1 , which perfectly reflects the selection criteria.

It should also be noted that the determination of the individual aggregate masses does not require any knowledge about the corresponding friction time, because for $\Delta t \ll \tau_i$ the Ornstein-Fürth relation [Eq. (1)] is approximated by Eq. (3), whereas determining the friction time is impossible without knowing the particle mass. Thus, any systematic error in the mass determination will cause a systematic error in the friction time, but not vice versa.

To control the consistency of the derived masses and response times in the two spatial directions x and y , we also show in Fig. 18 the relations between the masses m_x and m_y and translational response times $\tau_{t,x}$ and $\tau_{t,y}$, respectively. The correlation between the two individual mass measurements is very close over about three orders of magnitude of mass variations. A formal fit of $m_y = am_x + b$ yields $a = 1.02 \pm 0.02$ and $b = (0.5 \pm 4.0) \cdot 10^{-16}$ kg = $(0.02 \pm 0.12)m_0$, with a Pearson correlation coefficient of 0.968. In contrast, the correlation between $\tau_{t,x}$ and $\tau_{t,y}$ is rather weak, with a formal fit of $\tau_{t,y} = c\tau_{t,x} + d$, yielding $c = 0.87 \pm 0.07$ and $d = (1.2 \pm 0.5)$ ms, with a Pearson correlation coefficient of 0.882. However, this is mostly caused by the small range of values of τ_i , which span only a factor of about 3. As shown in Sec. IV A, the relative uncertainties in the determination of masses and response times are very similar.

Although the formal mass error is relatively small, we cannot resolve the discretization of the masses in the lower mass range (see inset of the top left of Fig. 18). This is mainly due to the monomer-mass uncertainty ($0.05 \mu\text{m}$ uncertainty in radius, i.e., $\pm 20\%$ uncertainty in monomer mass) [9,29], which leads to an overlap of the masses for neighboring mass

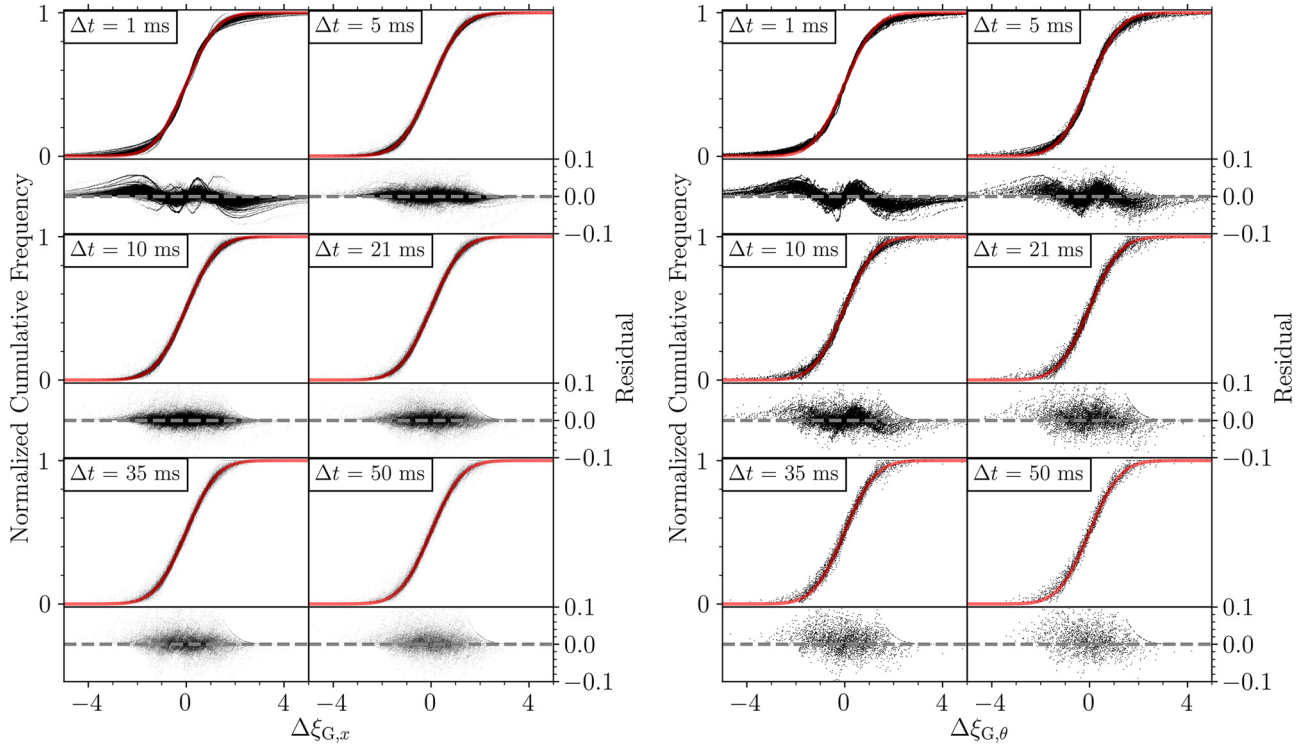


FIG. 16. Left: Same as Fig. 12, but showing the one-dimensional displacement data for all particles of the data set T1 after normalization following Eq. (17). The solid curves show the normalized error integrals [Eq. (18)]. Below each plot, the residuals are shown. Right: Rotational equivalent of the left figure, showing the normalized angular displacement data for all particles of data set R1.

units. Moreover, due to the higher Brownian velocities for the small masses, such particles move out of focus after a shorter time than massive aggregates. Due to this shorter trajectory length, the intrinsic uncertainty in the mass determination is larger for small masses.

APPENDIX D: EXCLUSION OF A SYSTEMATIC PARTICLE DRIFT

A possible systematic drift (parameters $\delta_x(j)$ in Eq. (16) and $\delta_\theta(j)$ for the rotational equivalent) from the analysis of the Brownian motion can either be real or an artifact of the fitting procedure. To test which of the two dominates in our data, we performed a statistical analysis of the parameters $\delta_x(j)$ in Eq. (16) and $\delta_\theta(j)$ in the rotational equivalent, which is shown in Fig. 19 as cumulative histograms for sampling times of $\Delta t = 1$ ms, 5 ms, 10 ms, and 50 ms, respectively. In the top row of Fig. 19, we can see that the absolute drift in x (left) and y directions (right) is almost symmetric to the zero value, with a maximum median value of $\sim 0.25 \mu\text{m}$ in the x direction for $\Delta t = 50$ ms (see inset of Fig. 19), equivalent to a median drift velocity of only $\sim 5 \mu\text{m/s}$. However, the total width of the distribution functions increases with increasing sampling time, but less than linear. If the drift was systematic and constant over the observation time, a linear relation between δ and Δt would be expected. Thus, we hypothesize that the drift is caused by the diffusion process itself. To test this, we plotted in the second row of Fig. 19 a cumulative normalized histogram of the values of $(\delta t_{\text{obs}})/(l_{\text{drift}} \Delta t)$. If the drift was a fitting-procedure artifact of the Brownian motion

itself, we would expect that the average overall drift length $l_{\text{drift}} \approx \sqrt{2D_t t_{\text{obs}}}$ scales with the square root of the observation time. This relation should be valid as long as $t_{\text{obs}} \gg \tau_t$ and $\Delta t > \tau_t$. Here, D_t and t_{obs} are the translational diffusion constant [Eq. (9)] and the overall observation time of the considered particle trajectory, respectively. We can see from the second row of Fig. 19 that all data collapse onto a single distribution function, regardless of the sampling time. Thus, we can conclude that there is no discernible external drift in the Brownian-motion data and that the small values of δ are a result of fitting a Gaussian to the particle displacements for trajectories whose end points do not coincide with their starting positions.

In bottom row of Fig. 19, the same type of diagrams are shown for the rotational Brownian motion. Here again, the distribution of δ_θ values gets wider with increasing sampling time, similar to the translational case (compare bottom left plot to the top row of Fig. 19). However, normalizing the rotational drift the same way as the translational shows that the width of the distribution function even decreases with increasing values of $(\delta_\theta t_{\text{obs}})/(l_{\text{drift},\theta} \Delta t)$. This is due to the rotational drift limit and the periodicity of the rotation angle, so also in the rotational case, the drift value can be explained by the Brownian motion itself.

APPENDIX E: DERIVING THE FRACTAL DIMENSION FROM OPTICAL DATA

As mentioned in Sec. IID, the information extracted from the images also include some data that are irrelevant to the

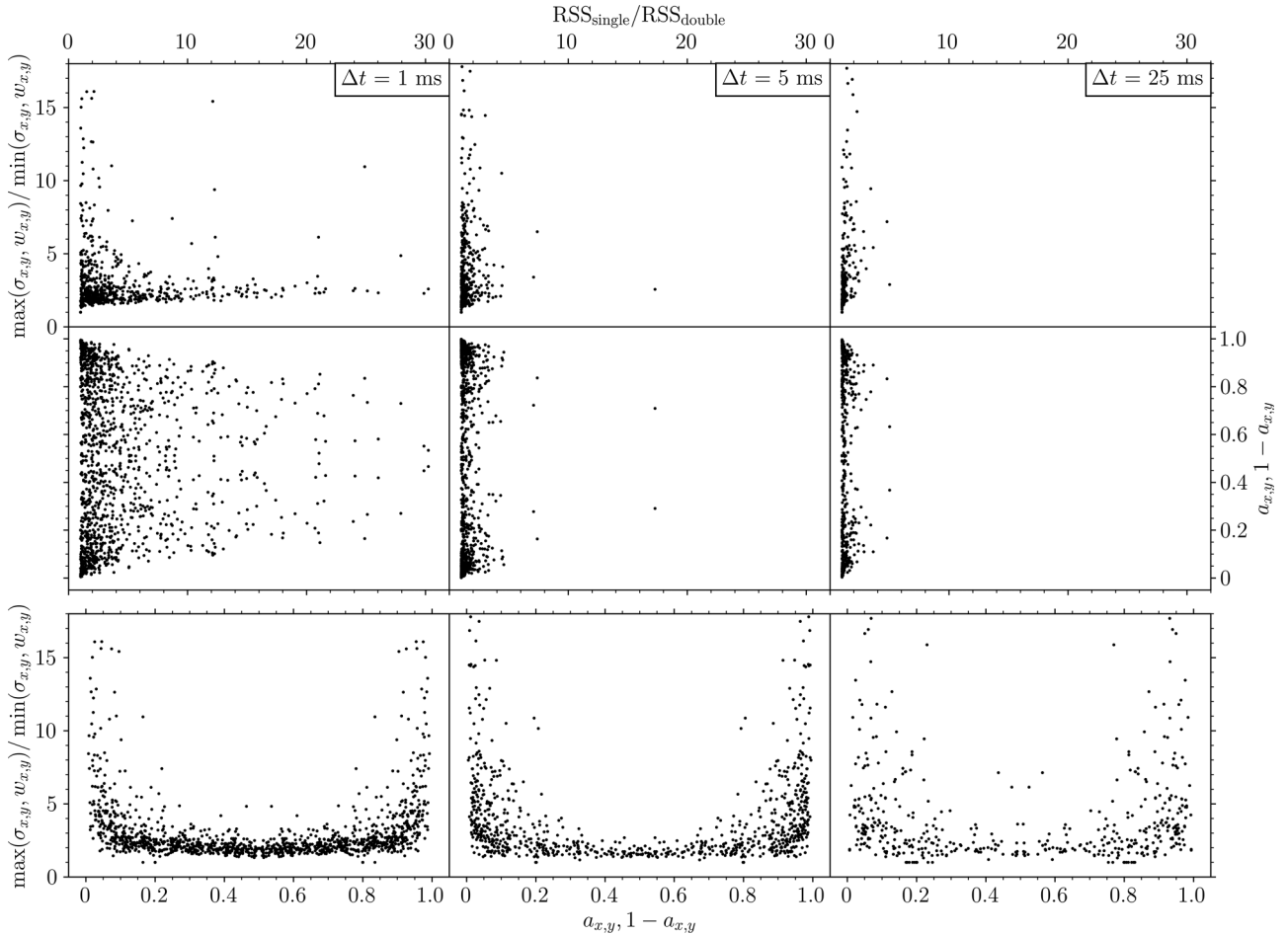


FIG. 17. Comparison of single-Gauss and double-Gauss fits and parameter ranges for the double-Gauss fit results for three values of the sampling time, $\Delta t = 1$ ms (left column), $\Delta t = 5$ ms (middle columns), and $\Delta t = 25$ ms (right column), using data set T1. The top row shows the width ratio of the two Gauss functions as a function of the RSS ratio for the two fit functions. The middle row displays the amplitudes of the two Gauss functions as a function of the RSS ratio for the two fit functions. The bottom row shows width ratio of the two Gauss functions as a function of their amplitudes.

Brownian motion analysis, namely, the two-dimensional radius of inertia and the total extinction, or optical mass, of a particle. The benefit of these data lies in the fact that they do not require the compensation of external drifts and are, thus, available for all experimental phases of ICAPS. However, due to image blurring, this data also requires careful calibration, which can be achieved using the correlations between mass and moment of inertia derived through Brownian motion analysis and those derived optically.

1. Mass correlation

On the left of Fig. 20, we show that, ignoring a few outliers, a strong correlation between the optical mass μ_{opt} and the mass derived from translational Brownian motion m_{BM} can be recognized. To account for a slight nonlinearity in light extinction, we applied the relation

$$\mu_{\text{opt}} = \kappa_0 \left(\frac{m_{\text{BM}}}{m_0} \right)^{\kappa_1}, \quad (\text{E1})$$

with m_0 being the monomer mass (see Sec. II B), and expect $\kappa_1 \approx 1$. After logarithmic fitting, we obtained the free parameters $\kappa_0 = 526.6 \pm 1.0$ and $\kappa_1 = 0.96 \pm 0.01$. The excellent quality of the fit can be seen in Fig. 20 (left, solid red curve and bottom residuals). By normalizing the aggregate mass to the monomer mass [see Eq. (E1)], we also obtained the absorption of a monomer grain $\mu_0 = \kappa_0$.

A comparison to a linear fit, i.e., $\kappa_1 = 1$ (see Fig. 20, left, dashed blue curve and top residuals), shows that the nonlinearity is indeed small, with a maximum deviation between the two fits curves of $\pm 10\%$.

2. Moment of inertia correlation

In contrast to the correlation between optical and Brownian mass, which is independent of the optical resolution, the optical moment of inertia suffers from finite-resolution and diffraction effects. Thus, the optical image is always blurred and, thus, slightly larger than the particle itself (see Fig. 20, right). If we assume that the real aggregate radius r is enlarged

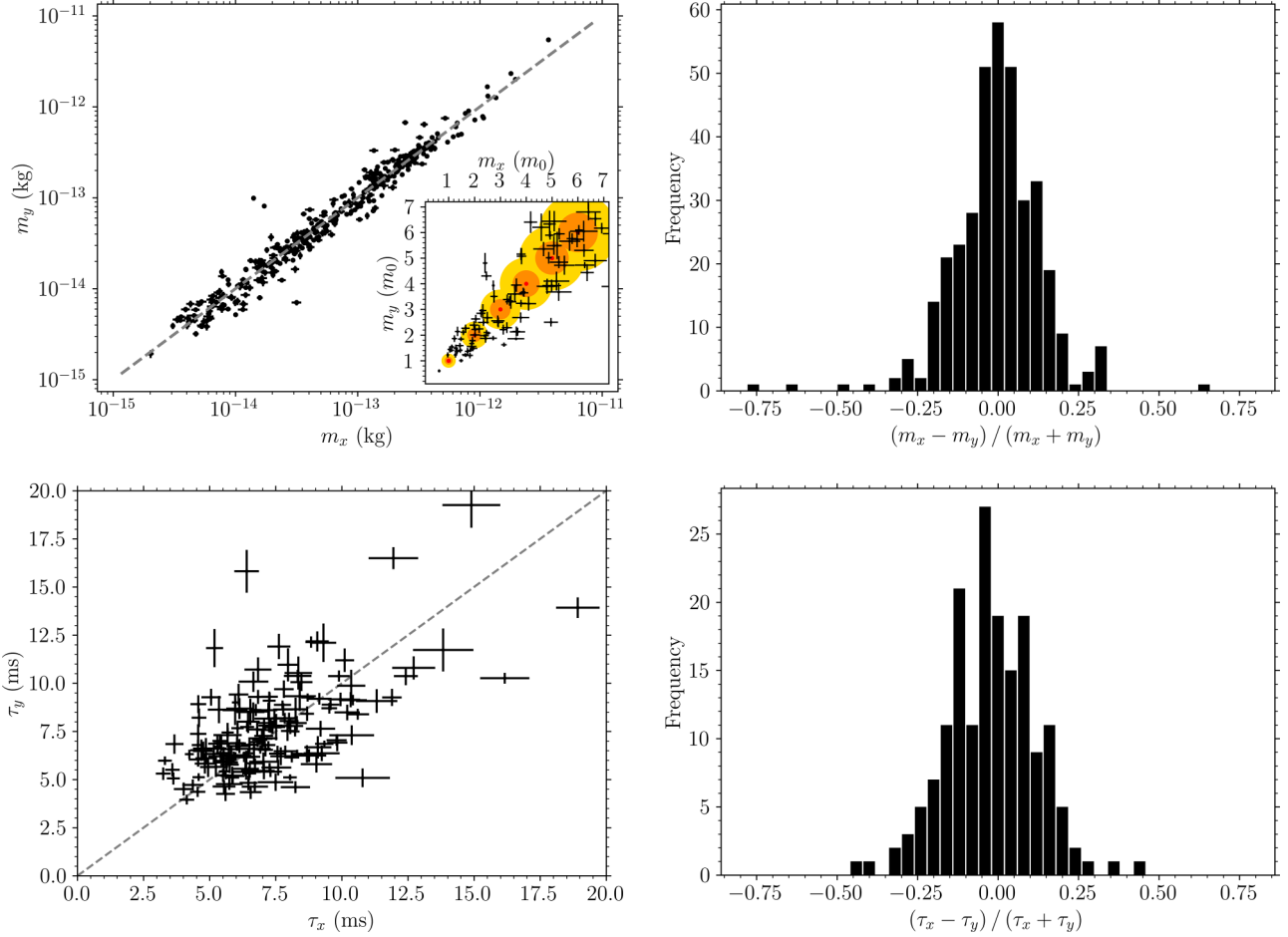


FIG. 18. Accuracy of the determination of masses and friction times. Top left: The correlation between the two mass measurements, m_x and m_y , for each particle in data set T1. The dashed line denotes $m_x = m_y$. The red dots in the inset denote the expected integer values of monomers, dimers, etc. The orange circles represent the error with respect to the dispersion of monomer radii and the yellow circles denote the doubled error. Top right: Histogram of the relative mass deviation between the x and y coordinates of the same particle. Bottom left: Response times $\tau_{i,y}$ measured with the one-dimensional displacement data in y direction versus $\tau_{i,x}$ measured in x direction for every particle in data set T2. The dashed line represents $\tau_{i,x} = \tau_{i,y}$. Bottom right: Histogram of the relative friction time deviation between the x and y coordinates of the same particle.

through these effects by a constant offset δr , i.e., the optical radius is $r_{\text{opt}} = r + \delta r$, the optical moment of inertia can be expressed by $i_{\text{opt}} \propto m r_{\text{opt}}^2 \propto m (r + \delta r)^2$. We can also assume that the optical mass is not affected by this effect, i.e., can be expressed by $m_{\text{opt}} \propto I_{\text{BM}}/r^2$, so we can relate the optical and the Brownian moment of inertia by $i_{\text{opt}} \propto \frac{I_{\text{BM}}}{r^2} (r + \delta r)^2 = I_{\text{BM}} (1 + \frac{\delta r}{r})^2$. Finally, combining Eqs. (12) and (11) results in $r \propto I_{\text{BM}}^{\frac{1}{2+d_f}}$ so we can apply the relation

$$i_{\text{opt}} = \lambda_0 \frac{I_{\text{BM}}}{I_0} \left(1 + \left(\frac{\lambda_1}{(I_{\text{BM}}/I_0)^{\lambda_2}} \right) \right)^2, \quad (\text{E2})$$

including the normalization to the moment of inertia of the monomers I_0 . As the fractal dimension and the radius enlargement are unknown quantities, we introduced free parameters. Fitting Eq. (E2) to the moments of inertia determined through optical and Brownian-rotation analysis, yields the three free parameters $\lambda_0 = (0.2 \pm 5.1) \times 10^{-11} \text{ counts} \cdot \text{m}^2$, $\lambda_1 = 20 \pm$

229, and $\lambda_2 = 0.09 \pm 0.13$, respectively. Figure 20 (right, solid curve and residuals) shows that Eq. (E2) fits the data very well and that a linear relation between i_{opt} and I_{BM} is inadequate see (Fig. 20, right, dash-dotted line). The inversion of Eqs. (E1) and (E2) allows the determination of the real masses and moments of inertia from their optical counterparts, though the latter requires numerical inversion.

3. Determination of the optical fractal dimension

As discussed in Sec. IVC2 and shown in Fig. 9, the Brownian motion analysis yielded a fractal dimension of $d_f = 1.40^{+0.08}_{-0.07}$. In comparison, the relation between the optical moment of inertia and the optical mass results in a fractal dimension of $d_f = 1.94^{+0.12}_{-0.10}$. After applying the calibrations through the Brownian-motion results [Eqs. (E1) and (E2)], the value of the fractal dimension becomes $d_f = 1.41^{+0.07}_{-0.06}$ (see Fig. 21). This value is within the errors identical to the one derived through the Brownian-motion data.

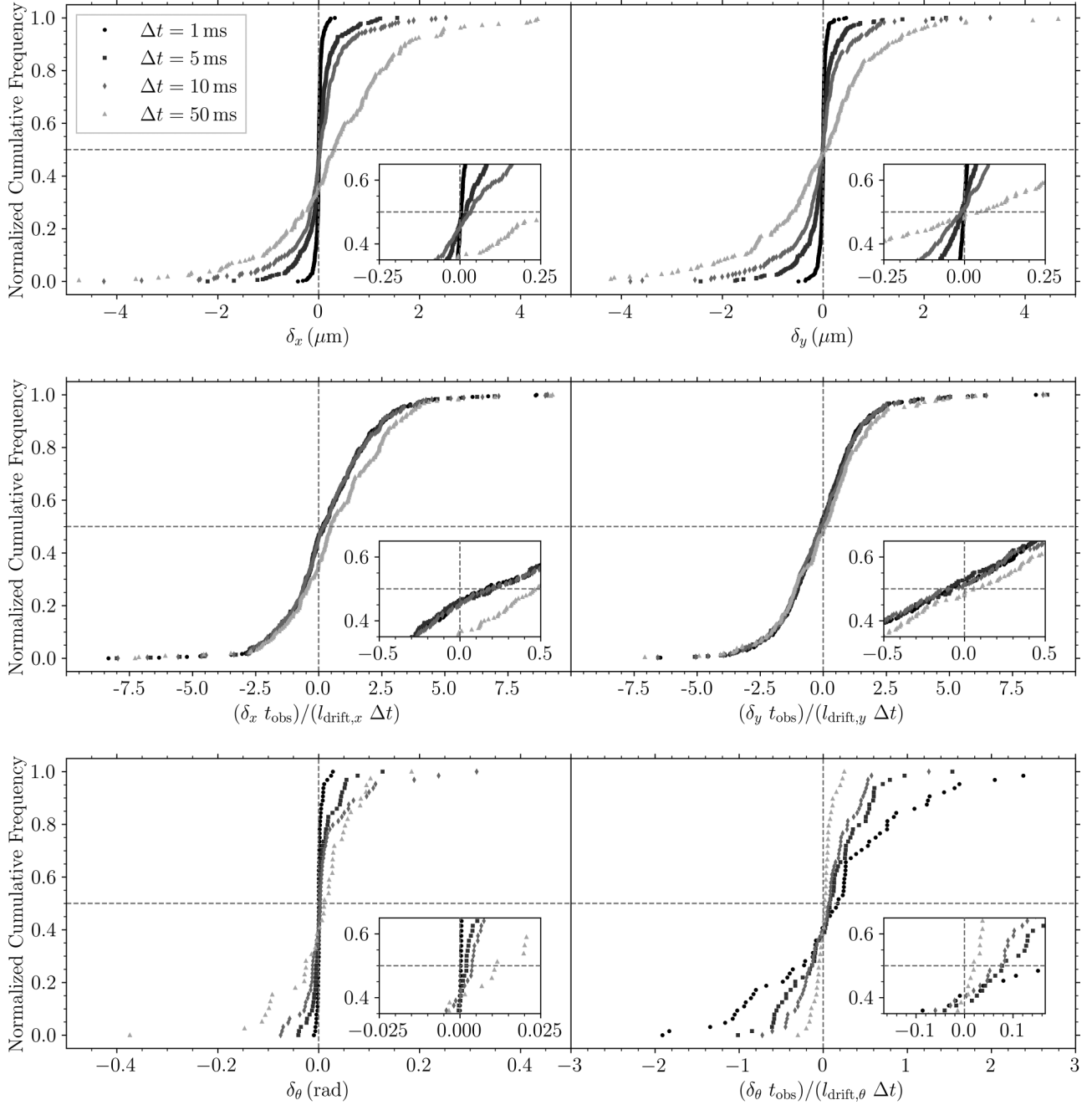


FIG. 19. Analysis of the values of the fit parameters $\delta_x(j)$, $\delta_y(j)$, and $\delta_\theta(j)$ in Eq. (16) for translation and its equivalent for rotation, respectively. Top row: Cumulative normalized histograms of $\delta_x(j)$ and $\delta_y(j)$ for four different sampling times, as indicated in the legend. Second row: Cumulative normalized histograms of $(\delta_x(j)t_{\text{obs}})/(l_{\text{drift},x}\Delta t)$ and $(\delta_y(j)t_{\text{obs}})/(l_{\text{drift},y}\Delta t)$, as described in the text. Bottom row: Same as above, but for rotation.

APPENDIX F: NOISE ANALYSIS

As shown in Sec. III A, the displacement data for the low Δt values show some systematic deviations from a Gaussian. In many cases, a combination of two Gaussians [see Eq. (B1)] delivers a much better fit to the observed data. In the following subsections, we seek for explanations of this unexpected behavior by identifying noise sources that can contribute to the observed effect.

1. Influence of cloud manipulation on the particle trajectories

In the levitation mode, the CMS feedback loop updates the Peltier control currents once per 20 ms. However, the temperature variation rate is limited by the thermal inertia of the Peltier elements. The measured response time of the CMS hardware was about $\tau_{\text{CMS}} = 100$ ms, so temperature variations with frequencies higher than $\sim 1/\tau_{\text{CMS}} = 10$ Hz were not present. From the housekeeping data of the CMS,

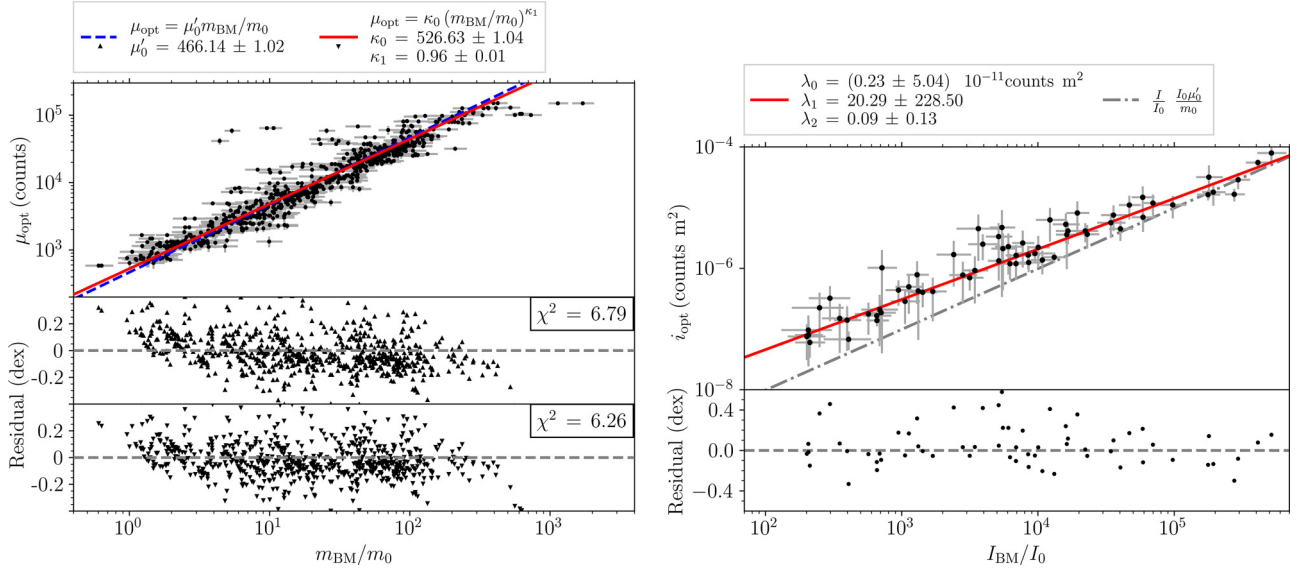


FIG. 20. Calibration of the imaging properties through the physical properties determined by Brownian motion. Left: Aggregate mass. The dashed blue line shows the best-fitting linear relation between the particle mass determined through the translational Brownian motion and the maximum total particle extinction for all particles in data set T1 in both x and y directions. The solid red line represents the best-fitting power law according to Eq. (E1). The two plots below represent the residuals. Right: Aggregate moment of inertia. The solid curve shows the best-fitting relation between the optical moment of inertia i_{opt} and the moment of inertia I_{BM} determined through the rotational Brownian motion for all particles in data set R1, according to Eq. (E2). For comparison, the dashed-dotted gray line marks a linear relation between i_{opt} and I_{BM} .

we reconstructed the mean active cloud shift as a function of time step Δt , which is shown as the red band in Fig. 2.

Due to small differences between individual Peltier temperatures for the same currents, the CMS caused a nonuniform creep motion of the dust cloud with average velocity of $\sim 50 \mu\text{m/s}$. This led to a cloud deformation with a timescale of minutes, which makes the effect negligible for the Brownian motion analysis.

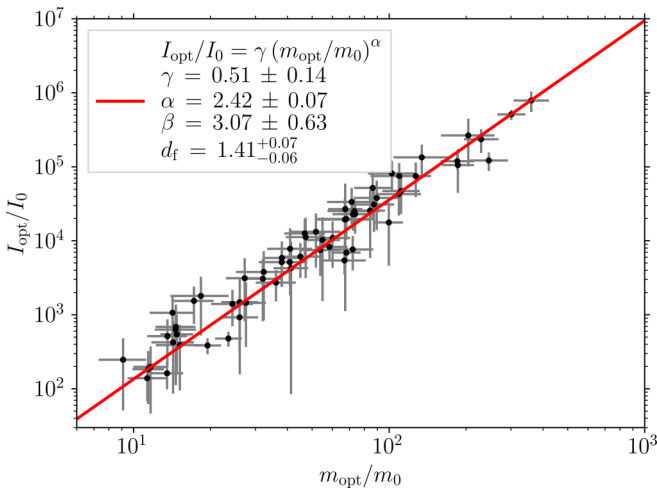


FIG. 21. Determination of the ensemble fractal dimension of data set R2, using optical data which was calibrated through their Brownian counterparts (see Fig. 20). A power-law fit is shown by the red line, yielding $d_f = 1.41$.

2. Correction of spatial and temporal brightness gradients in the raw images

During a period spanning 43.6 s between the first and second experiment runs, the dust cloud was lost with image recordings still on. This offered abundant data for the analysis of noise (see Appendix F3) as well as the creation of a flat-field image, which is shown in the bottom of Fig. 22. The background exhibits a static gradient with a decrease in brightness from left to right and in a circular pattern, most likely caused by the LDM lighting. There are also a few dark patches, probably caused by contaminants in the optical path of the LDM. By employing a flat-field correction, we compensated these patterns and inverted the images. The top of Fig. 22 also shows the temporal evolution of the mean gray value across all pixels of each raw image. There is a shallow incline for each experiment run, as well as an offset between the two. During the period where the cloud was lost, the mean stays rather constant, though noisy, at 190 ± 2 counts, where the error denotes the maximum deviation.

The increase in brightness over time is due to a thinning of the dust cloud and the offset between the two dust injections is caused by an increase of dust contamination of the chamber windows. The former is barely influenced by the particles in view, which is supported by the fact that singular pixels show the same trend in brightness, since the likelihood of them being crossed by a particle is low. Two linear fits, one for each experiment run, were then used to adjust the mean brightness of the flat-field image before correction. Prior to the localization of particles, however, we also set all gray values in the corrected images below 4 to 0 counts to remove any noise

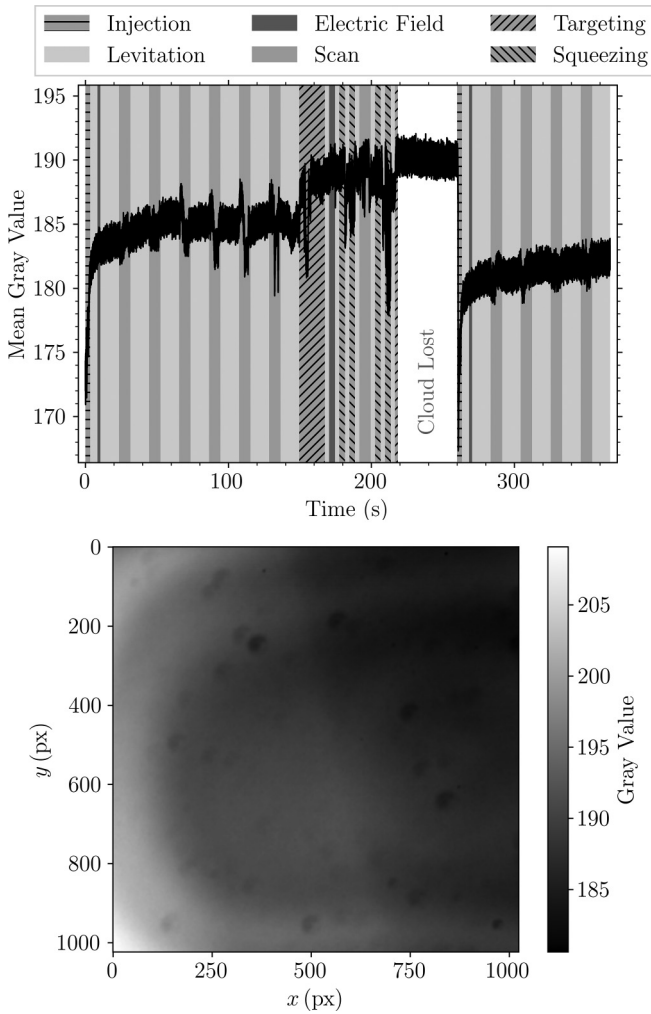


FIG. 22. Shot noise analysis. Top: Mean brightness across all pixels of each frame as a function of experiment time. Every experiment phase is marked with a different vertical band in the background. However, only the levitation phases were used for the Brownian motion analysis. Bottom: An average image recorded when the dust cloud was lost, which was then used as the flat-field image.

in the space between particles (see Appendix F3 for details on the noise).

3. Influence of optical noise on the measured particle positions and orientations

In any imaging system, there are sources of optical noise to consider. One such source is the discretization due to the finite distance between pixels. Also, the shot noise of the acquired images and fluctuations of the LDM illumination were taken into account here, which is not to say that there may not be other optical noise sources.

Since the shot noise of the camera should average to zero and the change in mean brightness, described in Appendix F2 and shown in the top of Fig. 22, is spatially homogeneous, the observed intensity noise (peaking at $\pm \sim 2$ counts) can be attributed to fluctuations (flickering) in the brightness of the LDM illumination. Analysis of the deviations from the

flat-field image (see bottom of Fig. 22) of each pixel in the dust-free period yielded a standard deviation for this effect of 0.63 counts. When adapting the mean brightness of the flat-field image to the momentary mean brightness, i.e., the flickering, before correcting the raw images (devoid of particles) with it, the remaining deviations can then be attributed to the shot noise. This yields a standard deviation of 0.35 counts.

With these parameters, a Monte Carlo simulation was then used to derive the offsets in the particle positions and orientations caused by the brightness flickering as well as the shot noise. For this, the respective Gaussian noise was applied to single-particle images with 100 random variations of the noise pattern per image. Following that, all relevant steps from the image analysis were implemented (e.g., the thresholding as described in Appendix F2). However, to also account for the aforementioned discretization noise, these images were actually produced in a Monte Carlo ray tracing simulation of artificial particles, which were grown in another simulation (see Appendix F4). Thus, the true center of mass was known and could be compared to the measurements after all the noise sources had been applied, which yielded the one-dimensional spatial offset caused by the sum of the optical noises.

In the rotational case, however, the orientation of the artificial particles was not well-defined and it was not possible to ensure high ellipticity (whose relevance is explained in Sec. IID). Thus, for the analysis of the rotational offsets we had to resort to particle images from the experiment, specifically to all particles in data set R1. We therefore cannot say how large the influence of the discretization is on the particle orientation, although the positional offsets from this noise seem to indicate that it is negligible. The other noise sources, i.e., shot noise and illumination flickering, most likely play a much greater role in the final rotational offsets. Since there might be a dependency on particle size, the median square absolute offsets were derived for each particle individually, yielding the upper and lower bounds in the left and right of Fig. 2 for translation and rotation, respectively.

4. Discretization noise induced by bright-field microscopy

Technically, the LDM used in this study for the determination of the particle properties is directly illuminated by the light source. Thus, all images appear bright, but no pixel of the CMOS sensor of the high-speed camera is saturated. When a particle is inside the field of view and within the depth of focus of the LDM, it appears darker than the background. Due to the nature of the SiO₂ particles used in this study, the darkening effect is entirely by diffraction and not by absorption. To simulate how stable the recorded center of extinction, which we assign to the center of mass of the aggregate, is under Brownian rotation of the aggregate around its center of mass as well as under random translational positioning of the pixel discretization grid, we performed Monte Carlo ray-tracing simulations.

In our ray tracing calculations, however, we modeled the extinction of light by assuming that the monomers were non-diffracting ($n = 1.0$) perfect spheres with a length absorption coefficient of $0.1 r_0^{-1}$, with r_0 being the monomer radius, which results in an effective extinction probability of 12 % for a ray randomly hitting a monomer. This effective extinction

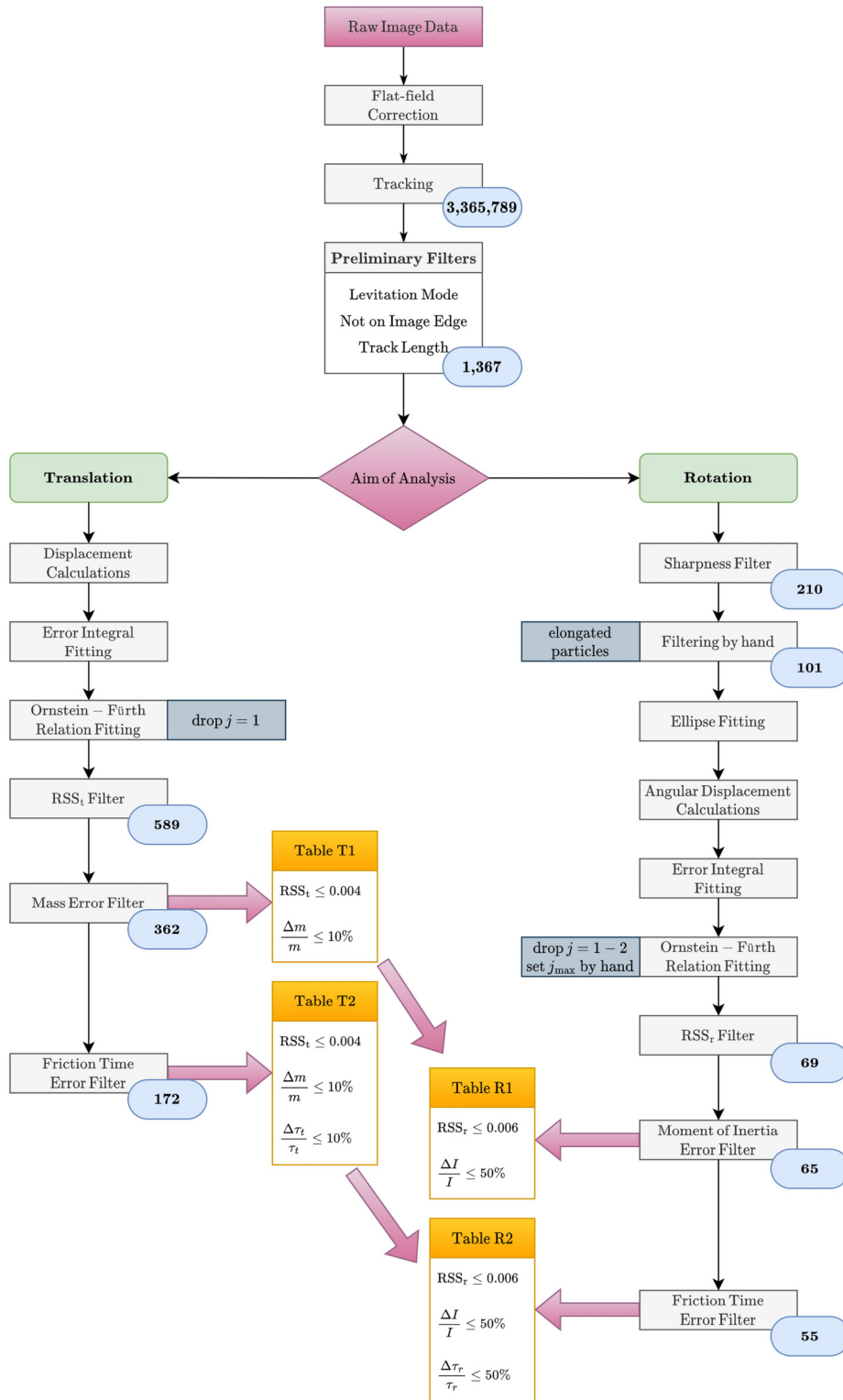


FIG. 23. Visualization of the data-analysis routines. On the left-hand side, the translational and on the right-hand side, the rotational Brownian motion analysis is shown. The number of remaining particles after each analysis step can be found in the blue ellipses.

probability is not based on data, but guessed, but we consider this setup sufficiently representative for the experiment, because light, when it interacts with a particle, has a certain probability to not impinge the CMOS sensor of the high-speed camera, depending on the amount of monomers it interacted with. Replacing nonabsorbing real by nonscattering simulated

particles has no effect on the outcome, but eases the Monte Carlo simulations quite considerably.

We assume the particles to be illuminated by light rays traveling in the z direction and starting at a random x, y position within a pixel. The number of starting rays per pixel is 190 counts, corresponding to the mean pixel brightness of

white images without particles observed in the experiment (see also Fig. 22, top). The light rays are then traced through the particle, where they can be extinguished according to the length absorption coefficient. Rays that did not get absorbed are counted behind the simulated particle, resulting in an image of pixel counts, just like in the experiment.

We calculated images of simulated BCCA particles (utilizing code by Bentley [26]) made of 2^1 to 2^9 (i.e., 2 to 512) monomers and random rotation axes around their centers of mass as a function of rotation angle in 1° steps. For each rotation step, the pixel grid behind the particle was placed with a random offset in x and y directions between zero and one pixel diameter to account for the translational motion of the particle. These ray tracing generated images as well as the particles' known centers of mass were then used for further noise analysis described in Appendix F 3.

5. Noise in the recording frequency of the high-speed camera

Although the internal clock of the high-speed camera is quartz driven, small frequency changes might occur. However, if this was the cause for the deviation from the perfect Gaussian in the one-dimensional Brownian motion, low-mass aggregates should, due to their higher Brownian velocities in the ballistic regime, exhibit a higher noise level than high-mass aggregates. This pattern was not found in the noise data, so we can exclude this noise source.

6. Rocket vibrations

In several previous microgravity experiments, particles exhibited substantial irregular non-Brownian displacements which were attributed to vibrations of the experimental chamber. The inertial random walk coefficient was introduced by Ilyukhin *et al.* [30] and the model was verified in ground-based experiments on ferromagnetic particles in the state of neutral buoyancy [31]. We investigated the importance of this phenomenon in the ICAPS experiment. The housekeeping data from the Texus-56 rocket showed that RMS vibrations were below 10^{-3} m s^{-2} , measured at a frequency of 40 Hz. We estimated the random-walk coefficient, the analogy of the Brownian diffusion coefficient, caused by these external vibrations, following the Rice method of spectral expansion from Langevin's equation [32] and assuming a constant gas-grain coupling time of $\tau_1 \approx 10 \text{ ms}$ for all particles. This resulted in an upper limit of vibration-induced mean-squared displacements at all sampling times of $\langle \Delta x^2 \rangle = 1.6 \times 10^{-15} \text{ m}^2$, lower than the measured signal (see Fig. 2).

APPENDIX G: FLOWCHART OF THE DATA ANALYSIS

Figure 23 provides a graphical overview of the data analysis applied to the ICAPS particles. For details, refer to Sec. II.

- [1] R. Brown, A brief account of microscopical observations made in the months of June, July, and August, 1827, on the particles contained in the pollen of the plants; and on the general existence of active molecules in organic and inorganic bodies, *Ann. Phys. Chem.* **90**, 294 (1828).
- [2] A. Einstein, On the movement of small particles suspended in a stationary liquid demanded by the molecular-kinetic theory of heat, *Ann. Phys.* **322**, 549 (1905).
- [3] M. von Smoluchowski, On the kinetic theory of the brownian molecular motion and of suspensions, *Ann. Phys.* **326**, 756 (1906).
- [4] G. E. Uhlenbeck and L. S. Ornstein, On the theory of the Brownian motion, *Phys. Rev.* **36**, 823 (1930).
- [5] J. Blum, G. Wurm, S. Kempf, and T. Henning, The Brownian motion of dust particles in the solar nebula: An experimental approach to the problem of pre-planetary dust aggregation, *Icarus* **124**, 441 (1996).
- [6] A. Vedernikov, N. Freuville, D. Balapanov, and A. Cecere, Cloud manipulation system Thermal characterization and drop tower experiment, *Proc. Int. Astro. Cong., IAC* **2**, 777 (2012).
- [7] J. Blum, G. Wurm, S. Kempf, T. Poppe, H. Klahr, T. Kozasa, M. Rott, T. Henning, J. Dorschner, R. Schräpler, H. U. Keller, W. J. Markiewicz, I. Mann, B. A. S. Gustafson, F. Giovane, H. Fechtig, E. Grün, D. Neuhaus, B. Feuerbacher, H. Kochan *et al.*, Growth and Form of Planetary Seedlings: Results from a Microgravity Aggregation Experiment, *Phys. Rev. Lett.* **85**, 2426 (2000).
- [8] M. Krause and J. Blum, Growth and Form of Planetary Seedlings: Results from a Sounding Rocket Microgravity Aggregation Experiment, *Phys. Rev. Lett.* **93**, 021103 (2004).
- [9] J. Blum, S. Bruns, D. Rademacher, A. Voss, B. Willenberg, and M. Krause, Measurement of the Translational and Rotational Brownian Motion of Individual Particles in a Rarefied Gas, *Phys. Rev. Lett.* **97**, 230601 (2006).
- [10] T. Poppe, J. Blum, and T. Henning, Generating a jet of deagglomerated small particles in vacuum, *Rev. Sci. Instrum.* **68**, 2529 (1997).
- [11] L. Waldmann, On the force of an inhomogeneous gas on small suspended spheres, *Z. Naturforsch., A* **14**, 589 (1959).
- [12] S. Beresnev and V. Chernyak, Thermophoresis of a spherical particle in a rarefied gas: Numerical analysis based on the model kinetic equations, *Phys. Fluids* **7**, 1743 (1995).
- [13] E. Hadamcik, J. B. Renard, J. Lasue, A. C. Levasseur-Regourd, J. Blum, and R. Schraepfer, Light scattering by low-density agglomerates of micron-sized grains with the PROGRA² experiment, *J. Quant. Spectrosc. Radiat. Transfer* **106**, 74 (2007).
- [14] J. Blum and R. Schräpler, Structure and Mechanical Properties of High-Porosity Macroscopic Agglomerates Formed by Random Ballistic Deposition, *Phys. Rev. Lett.* **93**, 115503 (2004).
- [15] G. Bradski, The OpenCV Library, *Dr. Dobb's Journal of Software Tools* (2000).
- [16] J. C. Crocker and D. G. Grier, Methods of digital video microscopy for colloidal studies, *J. Colloid Interface Sci.* **179**, 298 (1996).
- [17] D. Allan, C. van der Wel, N. Keim, T. A. Caswell, D. Wieker, and R. Verweij, soft-matter/trackpy: Trackpy v0.4.2 (2019).
- [18] Y. Feng, J. Goree, and B. Liu, Errors in particle tracking velocimetry with high-speed cameras, *Rev. Sci. Instrum.* **82**, 053707 (2011).
- [19] B. Wang, J. Kuo, S. C. Bae, and S. Granick, When Brownian diffusion is not Gaussian, *Nat. Mater.* **11**, 481 (2012).

- [20] micromed, Technical Datasheet: micromod Partikeltechnologie GmbH, <https://www.micromod.de>.
- [21] A. Squarcini, A. Solon, and G. Oshanin, Spectral density of individual trajectories of an active Brownian particle, *New J. Phys.* **24**, 013018 (2022).
- [22] T. Mukai, H. Ishimoto, T. Kozasa, J. Blum, and J. M. Greenberg, Radiation pressure forces of fluffy porous grains, *Astron. Astrophys.* **262**, 315 (1992).
- [23] C. Dominik and A. G. G. M. Tielens, The physics of dust coagulation and the structure of dust aggregates in space, *Astrophys. J.* **480**, 647 (1997).
- [24] J. Blum and G. Wurm, Experiments on sticking, restructuring, and fragmentation of preplanetary dust aggregates, *Icarus* **143**, 138 (2000).
- [25] D. Paszun and C. Dominik, The influence of grain rotation on the structure of dust aggregates, *Icarus* **182**, 274 (2006).
- [26] M. S. Bentley, aggregate, <https://github.com/msbentley/aggregate>.
- [27] See Supplemental Material at <https://link.aps.org/supplemental/10.1103/PhysRevE.107.034136> for movies showing the Brownian translation and rotation of particle 1 from Fig. 1.
- [28] G. Wurm and J. Blum, An experimental study on the structure of cosmic dust aggregates and their alignment by motion relative to gas, *Astrophys. J. Lett.* **529**, L57 (2000).
- [29] T. Poppe and R. Schräpler, Further experiments on collisional tribocharging of cosmic grains, *AAP* **438**, 1 (2005).
- [30] V. V. Ilyukhin, L. D. Iskhakova, V. F. Komarov, I. V. Melikhov, M. A. Prokofjev, V. K. Trunov, and A. A. Vedernikov, Peculiarities of crystallization process in the solution under microgravity (ERDENET experiment), *Acta Astronaut.* **11**, 651 (1984).
- [31] L. L. Regel, A. A. Vedernikov, R. V. Ilinski, and I. V. Melikhov, Analysis of inertial random walk of particles in liquids under microgravity conditions, in *Proceedings of the Sixth European Symposium on Material Sciences under Microgravity Conditions* (ESA SP-256, Bordeaux, France, 1987), Vol. 256, p. 593.
- [32] M. C. Wang and G. E. Uhlenbeck, On the theory of the Brownian motion II, *Rev. Mod. Phys.* **17**, 323 (1945).